# The Impact of Interactive Ocean Dynamics on Atlantic Sea Surface Temperature Variability

OLIVIA GOZDZ,[a] MARTHA W. BUCKLEY,[a] AND TIMOTHY DELSOLE[a]

[a] *George Mason University, Fairfax, Virginia*

(Manuscript received 5 October 2023, in final form 9 January 2024, accepted 12 February 2024)

ABSTRACT: The impact of interactive ocean dynamics on internal variations of Atlantic sea surface temperature (SST) is investigated by comparing preindustrial control simulations of a fully coupled atmosphere–ocean–ice model to the same atmosphere–ice model with the ocean replaced by a motionless slab layer (henceforth slab ocean model). Differences in SST variability between the two models are diagnosed by an optimization technique that finds components whose variance differs as much as possible. This technique reveals that Atlantic SST variability differs significantly between the two models. The two components with the most extreme enhancement of SST variance in the slab ocean model resemble the tripole SST pattern associated with the North Atlantic Oscillation (NAO) and the Atlantic multidecadal variability (AMV) pattern. This result supports previous claims that ocean dynamics are not necessary for the AMV, although ocean dynamics lead to slight increases in the memory of both the AMV and the NAO tripole. The component with the most extreme enhancement of SST variance in the fully coupled model resembles the Atlantic Niño pattern, confirming the ability of our technique to isolate physical modes known to require ocean dynamics. The second component with more variance in the fully coupled model is a mode of subpolar SST variability. Both the reemergence of SST anomalies and changes in ocean heat transport lead to increased SST variance and memory in the subpolar Atlantic. Despite large differences in the mean and variability of SST, atmospheric variability is quite similar between the two models, confirming that most atmospheric variability is generated by internal atmospheric dynamics.

KEYWORDS: Atlantic Ocean; Model comparison; North Atlantic Oscillation; Ocean dynamics; Oceanic variability; Sea surface temperature

## 1. Introduction

Atlantic sea surface temperature (SST) variations on decadal to multidecadal time scales have been linked to numerous climate phenomena in the Northern Hemisphere, such as changes in the frequency and intensity of Atlantic hurricanes, droughts in the Sahel, Arctic sea ice extent, and precipitation and temperature over adjacent landmasses (Folland et al. 1986; Enfield et al. 2001; Goldenberg et al. 2001; Sutton and Hodson 2005; Knight et al. 2006; Delworth et al. 2007; Ting et al. 2011; Day et al. 2012; Zhang 2015; Ruprich-Robert et al. 2017; Zhang et al. 2019). Thus, identifying the mechanisms behind decadal SST variations is crucial for providing reliable predictions of decadal variations. In this paper, we focus solely on the mechanisms of internally generated Atlantic SST variability and do not consider those generated by external forcing, such as aerosols (e.g., Booth et al. 2012; Undorf et al. 2018; Murphy et al. 2017; Bellomo et al. 2018).

A null hypothesis to explain SST variability in the mid- and high latitudes is the simple stochastic climate model of Frankignoul and Hasselmann (1977). In this framework, the ocean mixed layer integrates stochastic atmospheric forcing, resulting in a red spectrum of SST variability. SST anomalies are damped by air–sea heat fluxes with a damping time scale proportional to the mixed layer depth. The Frankignoul and Hasselmann null hypothesis has been successfully used to model extratropical SST variations and can serve as a benchmark to diagnose the contribution of other processes to SST variability, such as wind/buoyancy-driven ocean currents and ocean–atmosphere coupling (Manabe and Stouffer 1988; Seager et al. 2000, 2001; Pierce et al. 2001; Buckley et al. 2014, 2015).

The Frankignoul and Hasselmann (1977) model provides a framework by which spatial patterns of atmospheric variability can be imprinted upon the ocean. For example, tripolar SST anomalies seen in the North Atlantic are primarily the response to the North Atlantic Oscillation (NAO; Cayan 1992a,b), the dominant mode of atmospheric variability in the North Atlantic (Hurrell et al. 2003; Cook et al. 2019). A positive phase of the NAO is associated with stronger pressure differences between the subtropical high and subpolar low and a northward shift of the easterlies and westerlies. The wind anomalies reinforce the mean wind in the tropics and subpolar regions, leading to increased heat fluxes out of the ocean and negative SST anomalies. Wind anomalies oppose the mean wind in the subtropics, leading to reduced air–sea heat fluxes and warm SSTs. This pattern is commonly referred to as the NAO tripole pattern, and these anomalies are consistent with the Frankignoul–Hasselmann mechanism.

Denotes content that is immediately available upon publication as open access.

Supplemental information related to this paper is available at the Journals Online website: https://doi.org/10.1175/JCLI-D-23-0609.s1.

*Corresponding author*: Martha W. Buckley, marthabuckley@gmail.com

DOI: 10.1175/JCLI-D-23-0609.1

A natural question is whether SST patterns other than the NAO tripole can be explained by this stochastic climate model. Kushnir (1994) describes basinwide decadal SST patterns that do not appear to be forced by the overlying winds and asserts that these patterns are related to ocean dynamics. The basinwide nature and the decadal time scales of the SST anomalies described by Kushnir (1994) are now known as the Atlantic multidecadal variability (AMV; Kerr 2000; Knight et al. 2006; Gray et al. 2004; Knudsen et al. 2011; Mann et al. 2021). The AMV index is typically defined as SST anomalies averaged over the North Atlantic basin from 0° to 60°N with the global warming signal removed, either through linear detrending or regression (Enfield et al. 2001; Deser and Phillips 2021). Subsequent studies argue that multidecadal variations in the AMV arise from internal variations in the ocean, specifically the Atlantic meridional overturning circulation (AMOC; Zhang and Wang 2013; O'Reilly et al. 2016; Peings and Magnusdottir 2016; Delworth et al. 2017; Zhang 2017; Nigam et al. 2018; Oelsmann et al. 2020).

Clement et al. (2015) challenge the hypothesis that the ocean drives the AMV by showing that the AMV is similar between fully coupled models (FCMs) and sister slab ocean models (SOMs) in which the atmosphere interacts with a uniform 50-m depth motionless ocean. These results suggest that the Frankignoul–Hasselmann stochastic climate model, augmented by imposing structure of the stochastic forcing (e.g., NAO tripole pattern), primarily explains the AMV.

Clement's study set off a vigorous debate on the mechanisms of the AMV. Zhang et al. (2016) and O'Reilly et al. (2016) argue that, while the spatial pattern of the AMV in models without a dynamical ocean may be similar to that seen in coupled models, the mechanisms that give rise to AMV differ between models. Specifically, correlations between SST and air–sea heat fluxes change sign with time scale in the FCM, indicating that the atmosphere forces the ocean on short time scales, but ocean dynamics forces SST anomalies on decadal time scales. In contrast, the SOM SST anomalies are forced by the anomalous air–sea heat fluxes on all time scales (Zhang et al. 2016; O'Reilly et al. 2016). However, Cane et al. (2017) argue that correlations between low-pass-filtered SST and air–sea heat fluxes cannot be used to diagnose mechanisms, as even a small contribution from ocean dynamics can generate correlations that suggest that SST anomalies are forced by ocean dynamics. Zhang (2017) claimed that Cane's conclusions are invalid because they neglect ocean damping. Z. Liu et al. (2023) apply the Zhang (2017) model formulation to climate model simulations and observational data, finding that in both their model and in observations, the ocean forcing of the AMV is comparable with the atmospheric forcing. Furthermore, Schneider et al. (2023) suggest that the results of Cane et al. (2017) are based on the assumption that atmospheric and ocean dynamical forcings are uncorrelated, an assumption which is invalid for the real ocean. Delworth et al. (2017) used numerical experiments designed to explore the response to surface heat flux forcing related to the NAO in FCMs and sister SOMs (in the Geophysical Fluid Dynamics Coupled Model), concluding that AMV-like SST is driven by ocean dynamics in the FCM. Thus, the role of the ocean in Atlantic decadal SST variability remains a topic of vigorous debate, with a majority of studies focusing on the origin of the AMV.

In this paper, we determine which (if any) modes of Atlantic SST variability require interactive ocean dynamics. For this purpose, we follow Clement et al. (2015) and compare Atlantic SST between the FCM and SOM. However, instead of focusing on a single climate index like the AMV, we optimize a set of indices to maximally distinguish between the two models. The method for doing this is called covariance discriminant analysis (CDA; DelSole and Tippett 2022). Unlike studies that focus solely on the AMV, no filtering or preconceived ideas about the structure of the modes are imposed. Instead, CDA systematically identifies the patterns whose variance differs as much as possible between the two models.

## 2. Data

The datasets which we analyze are preindustrial control runs of Community Earth System Model version 1.2 (CESM1) FCM (Hurrell et al. 2013) and a sister SOM. For both the CESM1 FCM and SOM, we analyze 900 years of monthly output. Here, we describe these models in detail.

We use the CESM1 FCM in the same configuration as the Large Ensemble (LENS) project (Kay et al. 2015). The component models consist of the Community Atmosphere Model version 5 (CAM5, 30 vertical levels; Neale et al. 2010), the Parallel Ocean Program version 2 (POP2, 60 vertical levels; Smith et al. 2010; Danabasoglu et al. 2012a), the Community Land Model version 5 (CLM5; Lawrence et al. 2019), and the Los Alamos Sea Ice Model (CICE; Hunke 2010). All component models have approximately 1° horizontal resolution. Improvements to ocean model physical processes in POP2 [documented in Danabasoglu et al. (2012a)] include a new parameterization of density-driven overflows, which improves the penetration of North Atlantic Deep Water, as compared to observations (Danabasoglu et al. 2010).

Variability of the ocean circulation, in particular the AMOC, in preindustrial control simulations of CESM1 is described in Danabasoglu et al. (2012b, 2019). While we consider the preindustrial control simulations of CESM1, it is worth noting that comparisons between historical CESM1 simulations and observations show general model fidelity in the Atlantic basin (Danabasoglu et al. 2012b). The observed AMV spatial pattern is generally captured by regressions of the model-derived AMV index onto modeled SST, although the standard deviation of the simulated AMV and the low-frequency (multidecadal) power are too weak compared to observations (Kim et al. 2018).

The CESM1 SOM uses the same atmosphere and ice model as the FCM but is coupled to a motionless slab ocean on the atmospheric grid (Murphy et al. 2021). The slab layer depth at each grid point is set to be the corresponding annual average MLD from the FCM preindustrial control run (Fig. 1a). In contrast, the slab depth was specified to be 50 m everywhere in the CMIP3 SOMs analyzed in Clement et al. (2015); thus, the CMIP3 SOMs have too high a heat capacity in the tropics and too low a heat capacity at high latitudes. The CESM1 SOM has a mean heat capacity that is more consistent with the FCM than that of the CMIP3 SOMs.

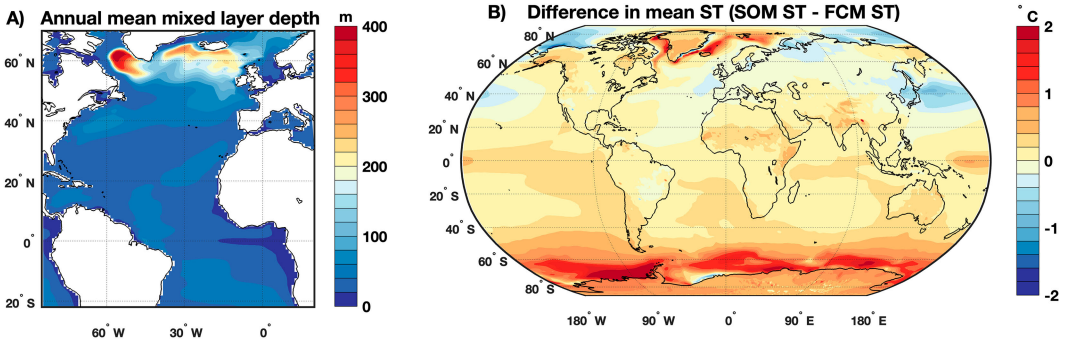


FIG. 1. (a) Annual mean mixed layer depth in meters for the CESM1 FCM calculated using the boundary layer depth (HBLT variable). The SOM configuration of CESM1 uses the time-average boundary layer depth as the slab layer depth. (b) The mean ST bias between the SOM and FCM (SOM ST − FCM ST).

To maintain a similar seasonal climatology of SST as in the FCM, the SOM implements a $Q$ flux, representing the seasonal climatology of ocean heat transport and mixing. From the mixed layer heat budget of the FCM,

$$Q_{\text{flux}} = Q_{\text{net}} - \rho c_p h_{\text{mix}} \frac{dT_{\text{mix}}}{dt}, \tag{1}$$

where $Q_{\text{net}}$ is the net surface heat flux, $h_{\text{mix}}$ is the MLD, $T_{\text{mix}}$ is the mixed layer temperature (assumed to be equivalent to SST), $\rho$ is the density of seawater, and $c_p$ is the specific heat of seawater. The seasonal climatology of $Q_{\text{flux}}$ is added to the energy balance equation in the SOM to maintain a mean and an annual cycle of SST in the SOM that is similar to the FCM. Despite this, the SOM has surface temperature (ST, equivalent to SST over the open ocean) biases of ~1° compared to the FCM (Fig. 1b).

Before proceeding, it is important to note that the SOM is missing both one-dimensional and three-dimensional oceanic processes. The SOM lacks (nonseasonal) variations in three-dimensional ocean currents and thus ocean heat transports. Additionally, the SOM lacks important one-dimensional processes related to seasonal and interannual MLD variations. The heat capacity of the SOM is too low in the winter and too high in the summer, resulting in unrealistic summertime persistence of SST anomalies (G. Liu et al. 2023). Because the SOM has a layer depth that is fixed in time, the SOM cannot simulate seasonal entrainment of waters.

To fairly compare the SOM and FCM, we need a common basis set. For this basis set, we chose to use empirical orthogonal functions (EOFs) from observational products. The use of observational EOFs is common for multimodel studies, especially because using any other EOF set would raise questions about whether the identified variability reflects that present in the ocean. For SST, we use EOFs calculated using monthly data (1945–2018) from Extended Reconstructed Sea Surface Temperature, version 5 (ERSSTv5). ERSSTv5 is a monthly 2° × 2° SST product that reconstructs SSTs (defined as near-surface temperatures from 0 to 5 m) from in situ ships, buoys, and Argo floats (Huang et al. 2017). For analysis of sea level pressure (SLP), we use monthly data (1948–2020) from the National Centers for Environmental Prediction (NCEP)–National Center for Atmospheric Research (NCAR) Reanalysis 1 project. The NCEP–NCAR reanalysis contains monthly atmospheric variables at a 2.5° × 2.5° resolution from 1948 to present and reconstructs variables using data from ships, buoys, rawinsonde, pibal, aircrafts, and satellites, among other data in conjunction with a state-of-the-art global data assimilation system (Kalnay et al. 1996).

## 3. Methodology

### a. Covariance discriminant analysis

Differences in variability between the two models are diagnosed by finding components whose variance differs as much as possible between the two models using a technique called CDA (DelSole and Tippett 2022). CDA maximizes variance ratios between two datasets; the resulting ratios are called discriminant ratios. We apply CDA to identify differences in SST and SLP variability between the SOM and FCM. Henceforth, the subscript $s$ will be used to denote quantities from the SOM and the subscript $c$ will be used to denote quantities from the FCM.

We first reduce the dimensionality of the problem by filtering the data using the leading EOFs from observations. For all EOF calculations, the Atlantic domain is defined to be the Atlantic Ocean between 30°S and 50°N; the northern boundary is at 50°N in order to avoid regions of sea ice. One of the most difficult aspects of CDA is deciding how many EOFs to retain, and details of how EOF truncations are chosen are presented in the appendix. Here, we retain 30 EOFs for both our SST and SLP CDA analyses.

CDA is computed between two matrices $\mathbf{F}_s$ and $\mathbf{F}_c$ obtained by multiplying the raw data from each model ($\mathbf{A}_s$ and $\mathbf{A}_c$) by the pseudoinverse of the observational EOFs (DelSole and Tippett 2022), henceforth referred to as $\mathbf{EOF}^\dagger$:

$$\underbrace{\mathbf{F}_s}_{[N,\,T]} = \underbrace{\mathbf{A}_s}_{[N,\,S]} \times \underbrace{\mathbf{EOF}^\dagger}_{[S,\,T]}, \tag{2a}$$

$$\underbrace{\mathbf{F}_c}_{[N,\,T]} = \underbrace{\mathbf{A}_c}_{[N,\,S]} \times \underbrace{\mathbf{EOF}^\dagger}_{[S,\,T]}, \tag{2b}$$

where $N$ is the number of time steps, $T$ is the number of EOFs, and $S$ is the number of spatial elements (i.e., number of grid points). We define a projection vector $\mathbf{q}_i$, which when

applied to $\mathbf{F}_s$ and $\mathbf{F}_c$, respectively, results in time series $\mathbf{r}_{s,i}$ and $\mathbf{r}_{c,i}$:

$$\mathbf{r}_{s,i} = \mathbf{F}_s\mathbf{q}_i, \tag{3a}$$

$$\mathbf{r}_{c,i} = \mathbf{F}_c\mathbf{q}_i. \tag{3b}$$

The terms $\mathbf{r}_{s,i}$ and $\mathbf{r}_{c,i}$ are referred to as the SOM variate time series and FCM variate time series, respectively.

The variance of each variate time series may be written as

$$\hat{\sigma}^2(\mathbf{r}_{c,i}) = \mathbf{q}_i^{\mathrm{T}}\hat{\mathbf{\Sigma}}_C\mathbf{q}_i, \tag{4a}$$

$$\hat{\sigma}^2(\mathbf{r}_{s,i}) = \mathbf{q}_i^{\mathrm{T}}\hat{\mathbf{\Sigma}}_S\mathbf{q}_i, \tag{4b}$$

where $\hat{\mathbf{\Sigma}}_C$ and $\hat{\mathbf{\Sigma}}_C$ are the sample covariance matrices in the coupled and slab models, defined as

$$\hat{\mathbf{\Sigma}}_C = \mathbf{F}_c^{\mathrm{T}}\mathbf{F}_c/N, \tag{5a}$$

$$\hat{\mathbf{\Sigma}}_s = \mathbf{F}_s^{\mathrm{T}}\mathbf{F}_s/N. \tag{5b}$$

CDA finds the $\mathbf{q}_i$ that maximizes the variance ratio:

$$\lambda_i = \frac{\hat{\sigma}^2(\mathbf{r}_{s,i})}{\hat{\sigma}^2(\mathbf{r}_{c,i})}. \tag{6}$$

This maximization problem leads to the eigenvalue problem:

$$\hat{\mathbf{\Sigma}}_S\mathbf{q}_i = \lambda_i\hat{\mathbf{\Sigma}}_C\mathbf{q}_i. \tag{7}$$

This eigenvalue problem yields $T$ eigenvalues, called discriminant ratios $\lambda_i$, that are ordered from largest to smallest. The corresponding eigenvectors solve the maximization problem in the sense that the first maximizes the variance ratio [Eq. (6)] among all possible vectors $\mathbf{q}_i$, the second maximizes the variance ratio such that the variates are uncorrelated with the first, and so on. The last eigenvalue $\lambda_T$ has the smallest variance ratio (and thus the largest variance in the FCM relative to the variance in the SOM). The $\mathbf{q}_i$ are defined up to a constant factor (e.g., multiplying $\mathbf{q}_i$ by a constant factor does not change $\lambda_i$). In CDA, it is standard to choose $\mathbf{q}_i$ to give $\hat{\sigma}^2(\mathbf{r}_{c,i}) = 1$, which necessarily implies $\hat{\sigma}^2(\mathbf{r}_{s,i}) = \lambda_i$.

Each component has a variance ratio $\lambda_i$ and an associated spatial pattern called a loading vector. The loading vector $\mathbf{p}_i$ can be obtained from linear regression using either $\mathbf{F}_s$ or $\mathbf{F}_c$, as we now show. The loading vector is the vector $\mathbf{p}_i$ such that $\mathbf{r}_{c,i}\mathbf{p}_i^{\mathrm{T}}$ best approximates $\mathbf{F}_c$ in a least squares sense. The solution is

$$\mathbf{p}_i = \mathbf{F}_c^{\mathrm{T}}\mathbf{r}_{c,i}(\mathbf{r}_{c,i}^{\mathrm{T}}\mathbf{r}_{c,i})^{-1} = \mathbf{F}_c^{\mathrm{T}}\mathbf{r}_{c,i}/N = \mathbf{F}_c^{\mathrm{T}}\mathbf{F}_c\mathbf{q}_i/N = \hat{\mathbf{\Sigma}}_C\mathbf{q}_i, \tag{8}$$

where we have used the fact that $\mathbf{r}_{c,i}$ is normalized to unit variance, and therefore, $\mathbf{r}_{c,i}^{\mathrm{T}}\mathbf{r}_{c,i}/N = 1$. Precisely, the same loading vector is obtained from $\mathbf{F}_s$:

$$\mathbf{p}_i = \mathbf{F}_s^{\mathrm{T}}\mathbf{r}_{s,i}(\mathbf{r}_{s,i}^{\mathrm{T}}\mathbf{r}_{s,i})^{-1} = \mathbf{F}_s^{\mathrm{T}}\mathbf{r}_{s,i}/(\lambda_i N) = \mathbf{F}_s^{\mathrm{T}}\mathbf{F}_s\mathbf{q}_i/(\lambda_i N) = \hat{\mathbf{\Sigma}}_S\mathbf{q}_i/\lambda_i$$
$$= \hat{\mathbf{\Sigma}}_C\mathbf{q}_i, \tag{9}$$

where we have used the fact that the variance of $\mathbf{r}_{s,i}$ is $\lambda_i$, and therefore, $\mathbf{r}_{s,i}^{\mathrm{T}}\mathbf{r}_{s,i}/N = \lambda_i$. The reader should keep in mind that CDA results in two variate time series, one for the SOM and one for the FCM, but only one spatial pattern.

Standard significance tests are not applicable in our problem because the model output is serially correlated. Accordingly, we adopt the following method to quantify significance. We split time series from the FCM and SOM in half and apply CDA to two halves of the same model. [The matrices $\mathbf{F}_s$ and $\mathbf{F}_c$ in Eqs. (2) and (3) are now two halves of the same model.] Results from two halves of the same model will be used to estimate the range of discriminant ratios under the null hypothesis of no change in the underlying stochastic process. If either the first or last discriminant ratios fall outside two standard deviations from the null cases, then we conclude that there is a significant difference in variability between the SOM and FCM.

Optimization may lead to discriminant ratios that are biased toward extreme values (i.e., far from 1) due to overfitting, as $\mathbf{q}_i$ is calculated using data contained in $\mathbf{F}_s$ and $\mathbf{F}_c$. Because of this, we compute an unbiased estimate of the discriminant ratio, called $\lambda_{iu}$, in which one-half of the data is used for finding $\mathbf{q}_i$ and the other half is used for calculating the discriminant ratio. Specifically, the projection vector is evaluated from one-half of the data [$\mathbf{F}_s^{(1)}$ and $\mathbf{F}_c^{(1)}$], and this projection vector [denoted as $\mathbf{q}_i^{(1)}$] is applied to the other half of the data [$\mathbf{F}_s^{(2)}$ and $\mathbf{F}_c^{(2)}$] to calculate unbiased estimates of the variate time series $\mathbf{r}_{s,i}^*$ and $\mathbf{r}_{c,i}^*$, where

$$\mathbf{r}_{s,i}^* = \mathbf{F}_s^{(2)}\mathbf{q}_i^{(1)}, \tag{10a}$$

$$\mathbf{r}_{c,i}^* = \mathbf{F}_c^{(2)}\mathbf{q}_i^{(1)}, \tag{10b}$$

We then compute the variance ratio as

$$\lambda_{iu} = \frac{\hat{\sigma}^2(\mathbf{r}_{s,i}^*)}{\hat{\sigma}^2(\mathbf{r}_{c,i}^*)}. \tag{11}$$

### b. *Divergence and total divergence*

From CDA, we can determine if the variability differs between two models, but the differences are distributed over $T$ discriminant components. Thus, there is a need to summarize overall model differences. Here, we introduce a quantity called divergence (Kullback 1997) that allows us to 1) determine the total model difference, 2) determine the portion of the total model difference explained by each component, and 3) determine the contributions of the mean state to the total model difference. It is worth noting that divergence explains only the total model difference which is captured by the EOF truncation.

For each discriminant component $i$, the divergence can be written as the sum of the parts due to differences in internal variability $D_{v_i}$ and differences in means $D_{m_i}$:

$$D_i = D_{v_i} + D_{m_i}. \tag{12}$$

The term $D_{v_i}$ is calculated from the $\lambda_i$ terms as

$$D_{v_i} = \lambda_i + \frac{1}{\lambda_i} - 2. \tag{13}$$

The term $D_{m_i}$ is equivalent to projecting the mean state differences onto the discriminant components and then taking the sum square:

$$D_{m_i} = \left(\frac{1}{\lambda_i} + 1\right)[\mathbf{q}_i^{\mathrm{T}}(\overline{\mathbf{F}}_c - \overline{\mathbf{F}}_s)]^2, \tag{14}$$

where $\overline{\mathbf{F}}_s$ and $\overline{\mathbf{F}}_c$ are the time mean $\mathbf{F}_s$ and $\mathbf{F}_c$ from Eq. (2).

The total model difference can be quantified using a scalar called the total divergence $\mathscr{D}$. The total divergence is the sum of the total divergence attributed to internal variability differences $\mathscr{D}_v$ and to differences in mean states $\mathscr{D}_m$ between the two models:

$$\mathscr{D} = \mathscr{D}_v + \mathscr{D}_m. \tag{15}$$

where

$$\mathscr{D}_v = \sum_{i=1}^{T} D_{v_i}, \tag{16a}$$

$$\mathscr{D}_m = \sum_{i=1}^{T} D_{m_i}. \tag{16b}$$

The fraction of the total divergence associated with each component is given by

$$P_i = \frac{D_i}{\mathscr{D}}. \tag{17}$$

## 4. Role of ocean dynamics in differences in monthly SST variance

### a. *Does the SST variability differ between the SOM and FCM?*

To begin with a familiar and simple comparison of ST variability, we show the natural logarithm of the local ST variance ratio (the SOM ST variance divided by the FCM ST variance) at each grid point for monthly data with the seasonal cycle removed (Fig. 2). Evaluating the significance of variance ratios poses challenges due to the serial correlation inherent in our time series, a condition unaccounted for by the standard $F$ test, which presupposes white noise. A frequently adopted solution is to perform the $F$ test utilizing an adjusted degree of freedom, one informed by the autocorrelation function. Determining the exact adjustment proves to be difficult, but our time series are so long that nearly any plausible estimate indicates significant variance ratios over most of the ocean. For instance, using 900 years of data and assuming a 2-yr $e$-folding decay time (which is shown to be consistent with autocorrelation functions of SST in section 4b) yields a 5%–95% interval of [0.86, 1.17]. Ratios residing within this interval are deemed insignificant and are stippled in Fig. 2.

Over most of the extratropical ocean, the SOM contains significantly higher ST variance than the FCM (Fig. 2). In the subpolar North Atlantic and off the coast of North America, the SOM has about 4.5 times the monthly variance of the FCM. In the tropical Atlantic, the FCM has more variance than the SOM, containing about 2 times the monthly ST variance.

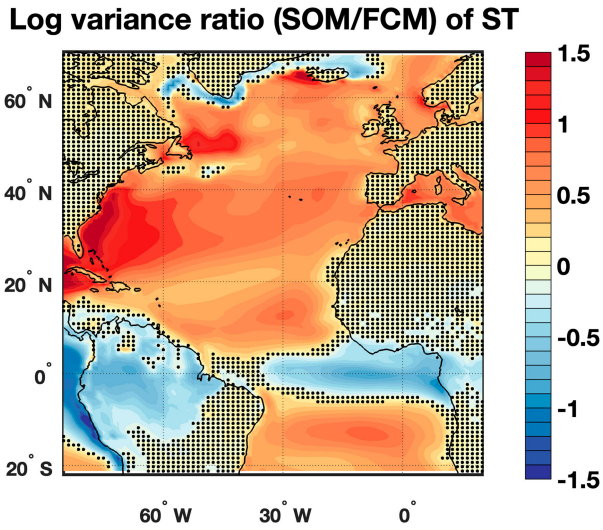


FIG. 2. The natural logarithm of the local ST variance ratio (the SOM ST variance divided by the FCM ST variance) at each grid point for monthly data with the seasonal cycle removed. Stippling indicates where the log ratios are *insignificant*.

The generally higher variance of the SOM compared to the FCM is due to the lack of oceanic damping in the SOM (Zhang 2017). A primary source of oceanic damping is the vertical entrainment of subsurface waters that occurs when the mixed layer deepens in the fall/winter, generally referred to as entrainment damping (Frankignoul 1985; Goodman and Marshall 1999; Frankignoul et al. 2002; Mignot and Frankignoul 2003). A recent study, which developed a stochastic model hierarchy and applied it to the FCM and SOM, demonstrates that entrainment is a key process that explains the reduced high-frequency SST variance in the FCM as compared to the SOM (G. Liu et al. 2023).

To ascertain if these SST variance differences can be explained by coherent patterns of variability, we apply CDA to monthly (deseasonalized) Atlantic SST in the FCM and SOM. As detailed earlier, we first filter the SST data using the leading EOFs calculated over the Atlantic Ocean between 30°S and 50°N. We use an EOF truncation of $T = 30$; the reason for and sensitivity to this EOF truncation choice is detailed in appendix (Fig. A1). The first 30 EOFs explain 86% of the Atlantic SST variance for the FCM and 91% of the SST variance for the SOM. The discriminant ratios (Fig. 3a) demonstrate that Atlantic SST variability in the SOM and FCM is significantly different. Overall, there are more components where the SOM has significantly larger variance ($\lambda_i > 1$) than components where the FCM has more variance ($\lambda_i < 1$). This is in line with the finding that the SOM generally has higher variance than the FCM (Fig. 2).

Now, we use divergence [Eqs. (12)–(14)] to quantify the relative importance of differences in the mean state (see mean

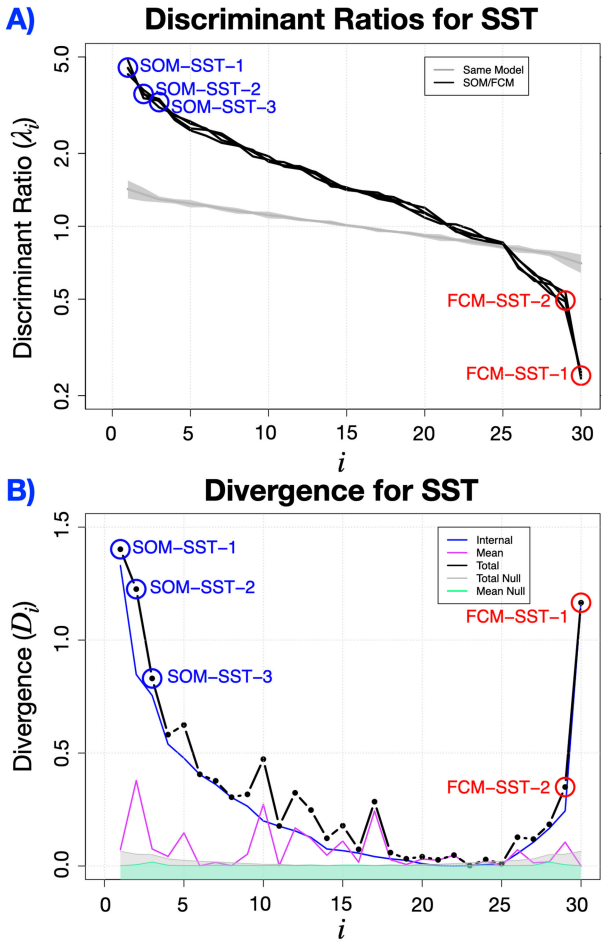


FIG. 3. CDA results comparing monthly Atlantic SST in the FCM and SOM. (a) Discriminant ratios as a function of the discriminant order for a 30-EOF truncation. The black lines show the leading discriminant ratios when the variance ratio of the SOM/FCM in Eq. (6) is maximized. The gray line shows the null hypothesis of equal variability using two halves from the same model (thick gray line is the mean and the gray shading shows the range of two standard deviations). (b) Divergence representative of the discriminant ratios. The black lines show the divergence ($D_i$), the purple lines shows the divergence due to the difference in means ($D_{m_i}$), and the blue lines denote the divergence due to differences in internal variability ($D_{v_i}$). The gray shading is the null hypothesis for divergence and the green shading denotes the null hypothesis line for the divergence due to the mean; both null cases are calculated using two halves from the same model.

ST difference between the FCM and SOM in Fig. 1b) and differences in internal variability. Significant differences in climatological SST exist between the FCM and SOM, but for most components, the divergence (Fig. 3b, black line) is dominated by differences in internal variability (Fig. 3b, blue line) rather than the mean state (Fig. 3b, purple line).

### b. *Components explaining SST differences*

In this section, we discuss in detail five components that differ significantly between the SOM and the FCM (these components are highlighted in Fig. 3). The three components with the most extreme enhancement of SST variance in the SOM are called SOM-SST-1, SOM-SST-2, and SOM-SST-3, respectively. SOM-SST-1 has 4.4 times more variance in the SOM than the FCM and explains 14% of the total divergence [calculated via Eq. (17)]. SOM-SST-2 has 3.4 times more variance in the SOM than the FCM and explains 12% of the total divergence. SOM-SST-3 has 3.2 times more variance in the SOM than the FCM and explains 8% of the total divergence. We remark that SOM-SST-2 and SOM-SST-3 have similar variance ratios and their ordering has some sensitivity to truncation choice (Fig. A1), indicating that these eigenmodes may not be separable. While one could choose to exclude both components due to separability concerns, we chose to include both components.

The two components with the most extreme enhancement of variance in the FCM are called FCM-SST-1 and FCM-SST-2, respectively. FCM-SST-1 has 4.1 times more variance in the FCM than in the SOM and explains 11% of the total divergence. FCM-SST-2 has 2.0 times more variance in the FCM than in the SOM and explains 3.5% of the total divergence. The pattern of FCM-SST-2 is somewhat sensitive to the EOF truncation choice (Fig. A1). The sensitivity to EOF truncation, as well as the relatively low variance ratio and divergence, suggests that FCM-SST-2 may not be robust. Together, these five components describe 49% of the total divergence between the SOM and FCM.

In the remainder of this section, we discuss each component in detail, including its spatial and temporal structure and the aspects of ocean dynamics that may explain the differences in variance between the SOM and the FCM. The spatial patterns associated with the leading SST components are given by the regression slope between the SST variate time series (independent variable) and atmospheric and oceanic fields of interest (dependent variable) at each grid point (Figs. 4, 6–8, 10, and 11). As discussed in section 3a, in CDA, it is standard to choose $\mathbf{q}_i$ to give $\hat{\sigma}^2(\mathbf{r}_{c,i}) = 1$ and $\hat{\sigma}^2(\mathbf{r}_{s,i}) = \lambda_i$. However, when presenting regression maps, it is attractive to compute regressions based on time series with unit variance, so that the squared regression coefficient equals the variance that is explained by the time series. Accordingly, when presenting regression maps, we first normalize variates to have unit variance and then compute regression coefficients using the normalized variates.

As discussed in section 3a, the same loading vector (spatial pattern) is obtained from regression of $\mathbf{r}_{s,i}$ onto $\mathbf{F}_s$ and $\mathbf{r}_{c,i}$ onto $\mathbf{F}_c$. Thus, when regressing normalized variate time series for the SOM and the FCM onto $\mathbf{F}_s$ and $\mathbf{F}_c$, respectively, one obtains spatial patterns that are exactly a factor of $\sqrt{\lambda_i}$ larger in the SOM. Regression patterns also may be computed from the raw (unfiltered) SST, $\mathbf{A}_s$ and $\mathbf{A}_c$, which differ from the loading vectors by including information from EOFs that were truncated in CDA. However, the regression patterns obtained with the EOF-truncated SST data and the raw SST data are nearly the same because the 30 EOFs explain the majority of the SST variance. For the figures presented in this paper, regression patterns computed from the raw data are shown. The pattern correlation (over the CDA domain) of regressions based on the FCM raw SST data and SOM raw SST

data is greater than 0.97 for all components analyzed here, implying that our EOF truncation is sufficient. Although our variate time series are derived for SST in the Atlantic region, the regression patterns can be evaluated globally. The regression slopes are calculated using CDA computed on the full 900-yr dataset.

### Components with more variance in SOM

The ST pattern for the component with the most extreme enhancement of SST variance in the SOM (SOM-SST-1, labeled in Fig. 3a) is tripolar in structure (Figs. 4b,c) and is related to a stronger response of SST to the NAO-like atmospheric variability in the SOM as compared to the FCM. Comparing regression maps of the SOM variate on SOM ST (Fig. 4b) and the FCM variate on FCM ST (Fig. 4c) shows that, as expected (see section 4b), the spatial structure is the same in both models (pattern correlation of 0.99 over the CDA domain), but the magnitude of the ST anomalies in the SOM is about two times larger than that in the FCM since $\sqrt{\lambda_1} = 2.1$. Power spectra of the (unnormalized) SOM and FCM variates (Fig. 5a) demonstrate that the SOM variate has more variance than the FCM variate at all frequencies, including low frequencies.

Regressions of the SOM variate and the FCM variate onto SLP show a weakened meridional climatological SLP gradient (Figs. 4d,e), which strongly resembles the negative phase of the NAO (Hurrell 1995). For a negative phase of the NAO, wind speeds are decreased in the equatorial and subpolar regions, leading to weaker heat fluxes out of the ocean (Figs. 4f,g) and warm SSTs (Figs. 4b,c). Wind speeds are increased in the subtropics, leading to increased heat fluxes out of the ocean (Figs. 4f,g) and cold SSTs (Figs. 4b,c). SOM-SST-1 shows a canonical forcing-response relationship with a box-based NAO index (Fig. S1a in the online supplemental material), although with modest correlations, which might be expected in comparing two indices derived from different physical variables (SST for SOM-SST-1 and SLP for the NAO) and different techniques (CDA for SOM-SST-1 and a box-based index for the NAO).

Unlike the ST regressions, the magnitudes of the SLP regression patterns are nearly identical for the SOM (Fig. 4d) and the FCM (Fig. 4e). Additionally, the $Q_{net}$ anomalies are somewhat weaker in the SOM (Fig. 4f) than in the FCM (Fig. 4g), implying that the larger SST variance in the SOM is not due to larger air–sea heat fluxes. These results suggest that the NAO-like atmospheric variability and associated air–sea heat fluxes are nearly the same in the two models, but the SST response in the FCM is muted relative to the response in the SOM. That is, ocean dynamics act to damp this atmospherically forced SST pattern. The ocean dynamical processes responsible for damping atmospherically forced SST variations in the FCM compared to those in the SOM are likely entrainment damping (see section 4a).

In addition to differences in total SST variance for SOM-SST-1, the SOM and FCM differ in the seasonal distribution of this variance (Fig. 5d). The (unnormalized) SOM variate has much higher variance than the (unnormalized) FCM variate in winter (more than 8 times more variance), while the differences in variance in fall are more modest (SOM variate has about 2 times more variance). Atmospheric variability is stronger in wintertime, and as a result, $Q_{net}$ has larger variance in winter than in summer in both the SOM and the FCM (Fig. S2). In the SOM, the layer depth is constant in time, so SST variance is also larger in wintertime as compared to summertime. In the FCM, several processes damp $Q_{net}$ variations, leading to a much smaller seasonal cycle of SST variance. The mixed layer is deeper in winter, so the atmospheric forcing is less efficient at changing SST, compensating for the larger wintertime variance of $Q_{net}$. Second, in the FCM, entrainment damps SST variability in fall and winter, as the mixed layer deepens.

The SOM and FCM also differ in their characteristic time scales of variability, as demonstrated by the seasonal autocorrelation function (ACF) of the FCM and SOM variate time series (Figs. 5g,j). The ACF is simply the correlation of time lagged data; a seasonal ACF starting at a given month is simply the ACF where lag = 0 is restricted to a given month. The SOM has unrealistically high summer persistence (Fig. 5g) due to weak summertime stochastic forcing distributed over an unrealistically deep layer (since the slab depth is set to be the annual mean MLD, which is deeper than the summertime MLD) (G. Liu et al. 2023). In contrast, the ACF from March of the FCM variate (Fig. 5g) initially decays rapidly, as the mixed layer shallows in summer resulting in more efficient damping and stochastic forcing. The seasonal ACF from March of the FCM variate shows a peak approximately 1 year later (Fig. 5g). This peak is likely a signature of reemergence of SST anomalies, in which SST anomalies formed during wintertime are isolated beneath the seasonal thermocline during summer and reemerge the following winter when mixed layers deepen, leading to enhanced persistence. The importance of reemergence in setting the characteristic time scale of the NAO tripole in observations was previously described by de Coëtlogon and Frankignoul (2003) and Sukhonos and Alexander (2023). The ACF from September of the FCM variate and the SOM variate is nearly identical (Fig. 5j), further suggesting that seasonal aspects dominate the differences between the FCM and SOM captured in SOM-SST-1.

A mode of variability which resembles the AMV emerges as the component with the second most extreme enhancement of SST variance in the SOM (SOM-SST-2); more details on the relationship between CDA components and the AMV are presented in section 4d. The spatial pattern of ST associated with the SOM and FCM variate time series has a characteristic horseshoe pattern (Figs. 6c,d; pattern correlation is 0.99 over the CDA domain); as expected, the amplitude of the pattern is about 2 times stronger in the SOM than in the FCM ($\sqrt{\lambda_2} = 1.8$). The SLP anomalies associated with the SOM and FCM variate time series are nearly identical (Fig. S3), implying that the atmospheric variations associated with SOM-SST-2 are the same in the SOM and the FCM, but the response of the ocean is different.

Typically, ocean dynamics are implicated in SST variability on longer time scales. As a result, we now examine whether SOM-SST-2 has more variance in the SOM than in the FCM at low frequencies or if the higher variance in the SOM is restricted to high frequencies. Power spectra of the unnormalized

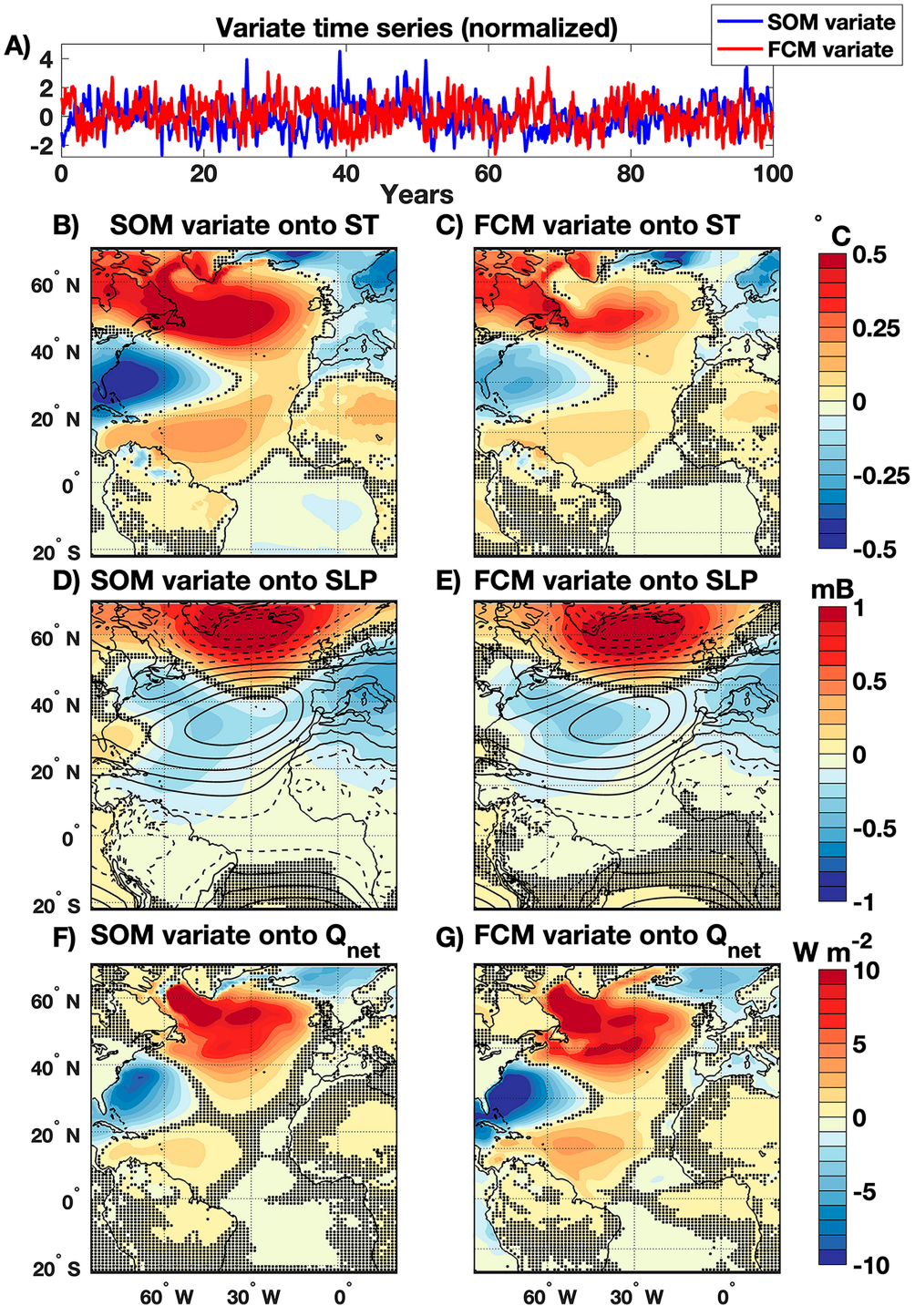


FIG. 4. The leading component with enhanced SST variance in the SOM (SOM-SST-1; Fig. 3a). (a) A 100-yr sample of the leading SOM variate (blue) and FCM variate (red) time series. The regression slope between the normalized SOM variate and (b) ST, (d) SLP, and (f) $Q_{net}$. The regression slope between the normalized FCM variate and (c) ST, (e) SLP, and (g) $Q_{net}$. The dots in (b)–(g) show where the regression is not significant at the 95% confidence level. In (d) and (e), the mean SLP field is shown in black contours with a contour interval of 2 mb (1 mb = 1 hPa). The solid and dashed contours indicate SLP values above and below the standard average pressure at sea level (1013.25 mb), respectively. Regressions are computed with $Q_{net}$ 1 month prior to the variate time series. Positive $Q_{net}$ means ocean gains heat from atmosphere.

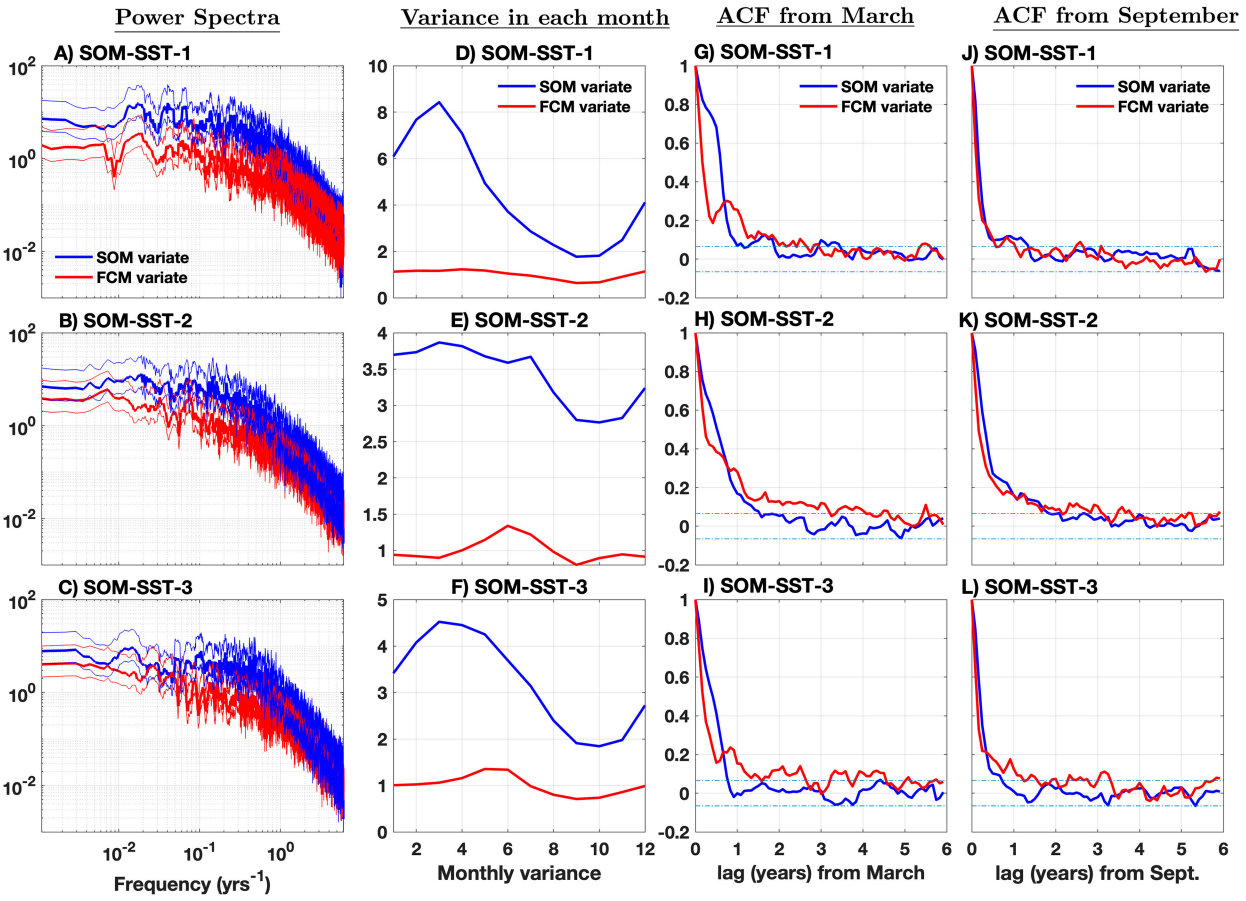


FIG. 5. Power spectra, variance distribution with month, and seasonal ACFs of the variate time series from the three components with higher variance in the SOM. Power spectra of the unnormalized SOM variate (blue) and FCM variate (red) for (a) SOM-SST-1, (b) SOM-SST-2, and (c) SOM-SST-3. The thick lines are the power spectral density, and the thin lines are the 95% confidence interval of the power spectra. The variance of the unnormalized SOM variate (red) and FCM variate (blue) as a function of month for (d) SOM-SST-1, (e) SOM-SST-2, and (f) SOM-SST-3. Seasonal ACF from March of the SOM variate (blue) and FCM variate (red) for (g) SOM-SST-1, (h) SOM-SST-2, and (i) SOM-SST-3. Seasonal ACF from September of the SOM variate (blue) and FCM variate (red) for (j) SOM-SST-1, (k) SOM-SST-2, and (l) SOM-SST-3. The dash-dotted blue lines in (g)–(l) indicate the level of correlations that are significantly different from zero at the 95% confidence level.

FCM variate and unnormalized SOM variate for SOM-SST-2 (Fig. 5b) demonstrate that the SOM variate has more variance than the FCM variate at all frequencies, including low frequencies. The SOM variate has more variance in the spring and less in the fall (Fig. 5e) due to the larger winter-season $Q_{net}$ variations. In contrast, the FCM variate has more variance in summertime (Fig. 5e), as a result of $Q_{net}$ variations being distributed over the shallow summertime mixed layer and the reduction of SST variance in the fall/winter due to entrainment damping. Modes with horseshoe structures that have maximal variance in the summertime have been described previously (Cassou et al. 2004; Wen et al. 2005; Frankignoul and Kestenare 2005; Gastineau and Frankignoul 2014).

The SOM variate and the FCM variate of SOM-SST-2 differ in memory, but only during the wintertime season. The seasonal ACFs from September of the FCM variate and the SOM variate are nearly identical (Fig. 5k). The seasonal ACF from March shows an initially more rapid decay in the FCM than in the SOM (Fig. 5h). In the FCM, memory is quickly lost in summer due to the formation of the seasonal thermocline, while the SOM has unrealistically high summer persistence. The ACF of the FCM variate is larger than the ACF of the SOM variate for lags greater than 1 year, and there is no sign of seasonal reemergence of SST anomalies. These results suggest that three-dimensional ocean dynamics may play a role in enhancing interannual memory in the FCM (Zhang et al. 2016; O'Reilly et al. 2016; Delworth et al. 2017; Li et al. 2020; Oelsmann et al. 2020), although the enhanced memory in the FCM is modest and seasonally dependent.

The component with the third most extreme enhancement of SST variance in the SOM (SOM-SST-3) is also tripolar in structure (Figs. 7b,c, pattern correlation of the SOM pattern and the FCM pattern is 0.99 over the CDA domain). However, the tripole is shifted northward compared to SOM-SST-1, with the middle lobe of the tripole centered off the Grand Banks. A similar SST pattern to SOM-SST-3 was previously isolated

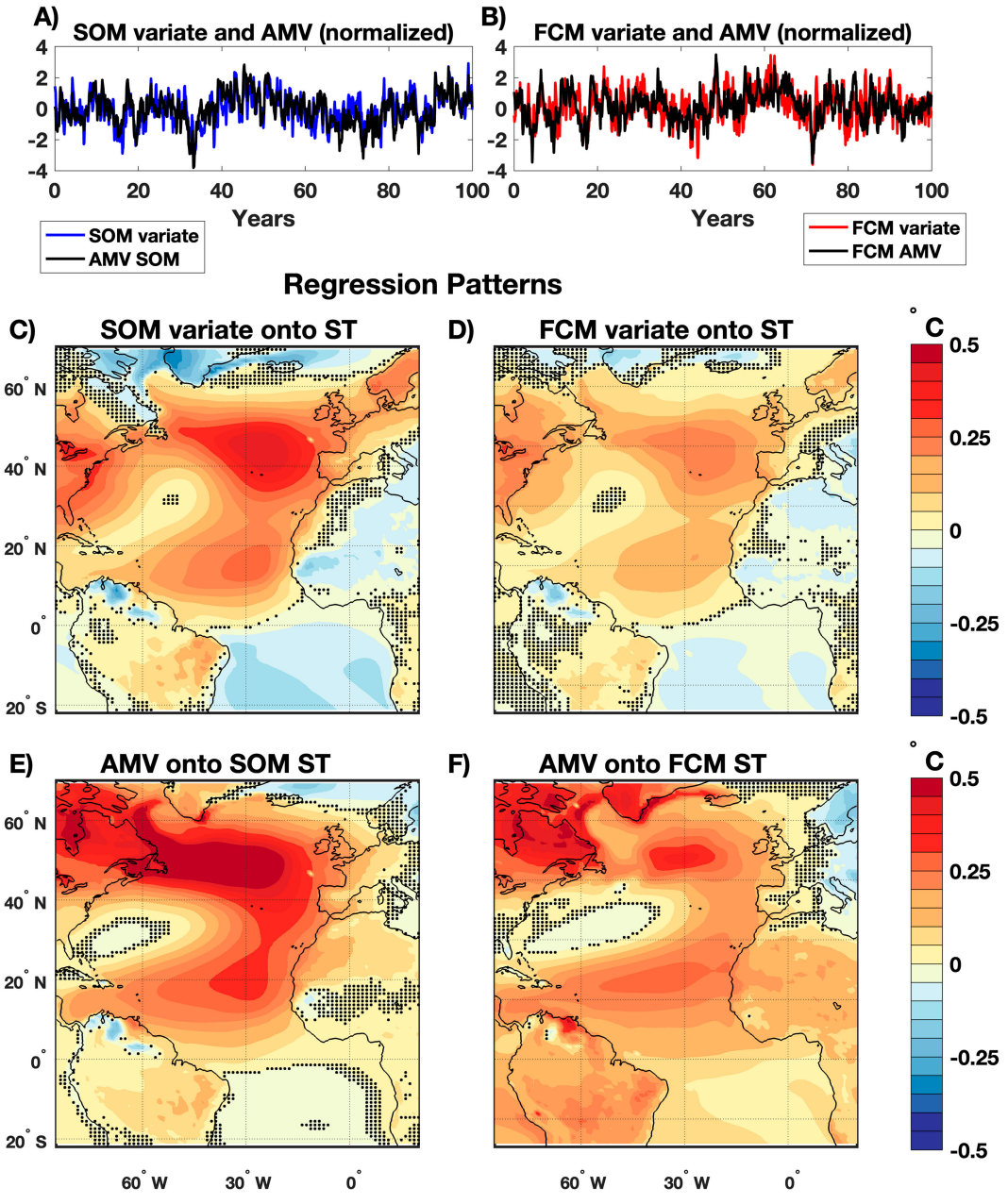


FIG. 6. The second leading component with enhanced SST variance in the SOM (SOM-SST-2; Fig. 3a). (a) A 100-yr sample of the normalized SOM variate (blue) and the normalized SOM AMV index (black); the correlation between these two time series is $\rho = 0.76$. (b) A 100-yr sample of the normalized FCM variate (red) and the normalized FCM AMV index (black); the correlation between these two time series is $\rho = 0.63$. (c) Regression slope between the normalized SOM variate and SOM ST. (d) Regression slope between the normalized FCM variate and FCM ST. (e) Regression slope between the normalized SOM AMV index and SOM ST. (f) Regression slope between the normalized FCM AMV index and FCM ST. In (c)–(f), the dots indicate where the regression is *not significant* at the 95% confidence level.

as the second EOF of North Atlantic SST [Figs. 3b,d of Buckley et al. (2014) and Fig. 5b of de Coëtlogon and Frankignoul (2003)]. As expected, the amplitude of the pattern is about 2 times stronger in the SOM than the FCM ($\sqrt{\lambda_3} = 1.8$). Similar to SOM-SST-1 and SOM-SST-2, SOM-SST-3 is associated with SLP anomalies of similar pattern and amplitude in the SOM and FCM (Figs. 7d,e). These results again suggest that the atmospheric variability is nearly the same in the two models, but the SST response in the FCM is muted relative to the response in the SOM.

Power spectra of the (unnormalized) SOM and FCM variates (Fig. 5c) demonstrate that SOM variate has more variance than the FCM variate at all frequencies, including low

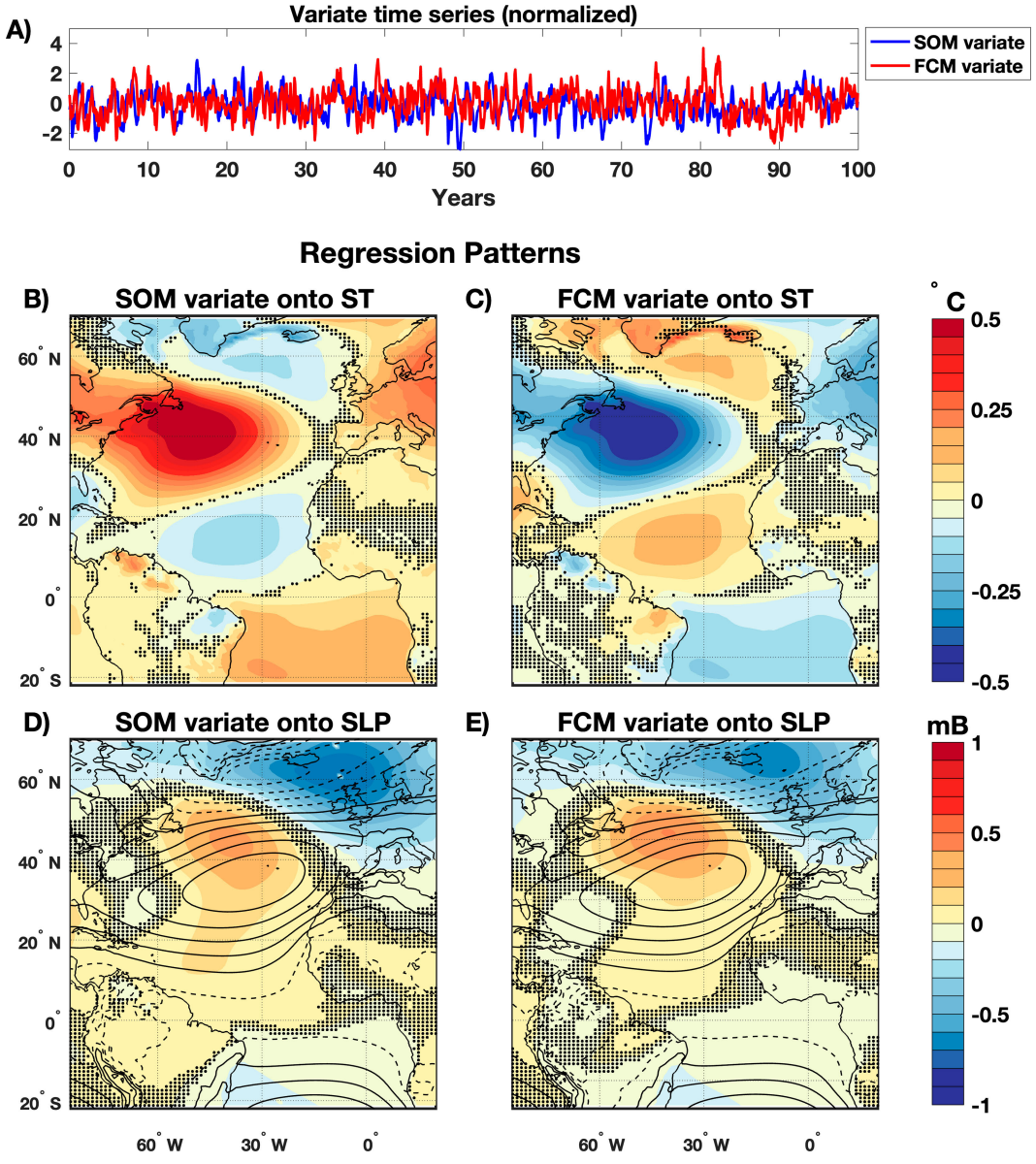


FIG. 7. The third component with enhanced SST variance in the SOM (SOM-SST-3; Fig. 3a). (a) A 100-yr sample of the normalized SOM variate (blue) and FCM variate (red) time series. The regression slope between the normalized SOM variate and (b) ST and (d) SLP. The regression slope between the normalized FCM variate and (c) ST and (e) SLP. The dots in (b)–(e) show where the regression is not significant at the 95% confidence level. In (d) and (e), the mean SLP field is shown in black contours with a contour interval of 2 mb. The solid and dashed contours indicate SLP values above and below the standard average pressure at sea level (1013.25 mb), respectively.

frequencies, although there is significant overlap between the 95% confidence levels of the spectra. Similar to SOM-SST-1, the variance differences are greater in winter (when the SOM has up to 4.5 times more variance than the FCM) than in fall (when the SOM has about 2 times more variance than the FCM; Fig. 5f). Differences in the seasonal ACFs of the SOM and FCM variates are modest, with signatures of enhanced summertime persistence in the SOM and enhanced interannual persistence in the FCM (Figs. 5i,l).

### c. *Components with more variance in the FCM*

We now shift focus and discuss components that have more SST variance in the FCM. A mode of variability that strongly resembles Atlantic Niño emerges as the component with the most extreme enhancement of SST variance in the FCM (FCM-SST-1). Regression of the FCM variate time series onto FCM ST (Fig. 8c) and the SOM variate onto SOM ST (Fig. 8d) results in patterns (pattern correlation is 0.97 over the CDA domain) that resembles that of the Atlantic Niño

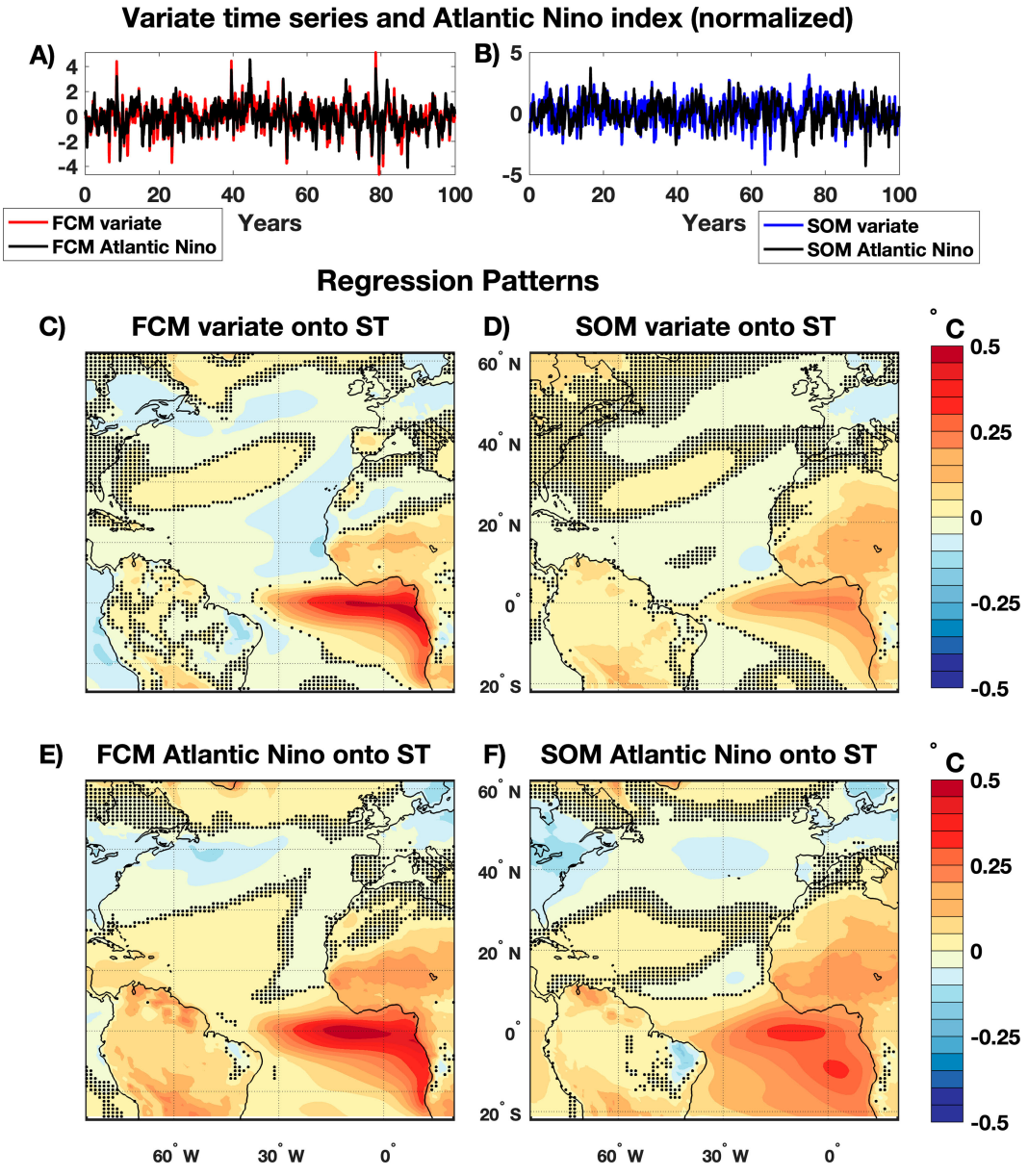


FIG. 8. The leading component with enhanced SST variance in the FCM (FCM-SST-1, Fig. 3a). (a) A 100-yr sample of the normalized FCM variate (red) and the normalized FCM Atlantic Niño index (black), defined as the SST anomalies in the tropical Atlantic located between 3°N–3°S and 20°W–0° (Zebiak 1993). The FCM variate and the FCM Atlantic Niño index have a correlation coefficient of $\rho = 0.85$. (b) A 100-yr sample of the normalized SOM variate (blue) and the normalized SOM Atlantic Niño index (black). The SOM variate and the SOM Atlantic Niño index have a correlation coefficient of $\rho = 0.58$. (c) Regression slope between the normalized FCM variate and FCM ST. (d) Regression slope between the normalized SOM variate and SOM ST. (e) Regression slope between the normalized FCM Atlantic Niño index and FCM ST. (f) Regression slope between the normalized SOM Atlantic Niño index and SOM ST. In (c)–(f), the dots indicate where the regression is not significant at the 95% confidence level.

(Figs. 8e,f), but the pattern has half the amplitude in the SOM, as $\sqrt{\lambda_{30}} = 0.5$.

The correlation between the FCM-SST-1 variate time series and box-based Atlantic Niño indices is $\rho = 0.85$ in the FCM (Fig. 8a) and $\rho = 0.58$ in the SOM (Fig. 8b). The box-based Atlantic Niño index has 2 times more variance in the FCM than in the SOM. Regression patterns for ST based on the box-based Atlantic Niño index are stronger and more concentrated on the equator in the FCM (Fig. 8e) and more diffuse in the SOM (Fig. 8f). Prior studies have pointed out the presence of weak ENSO-like variability in models with only thermodynamic coupling (Dommenget 2010; Clement et al. 2011;

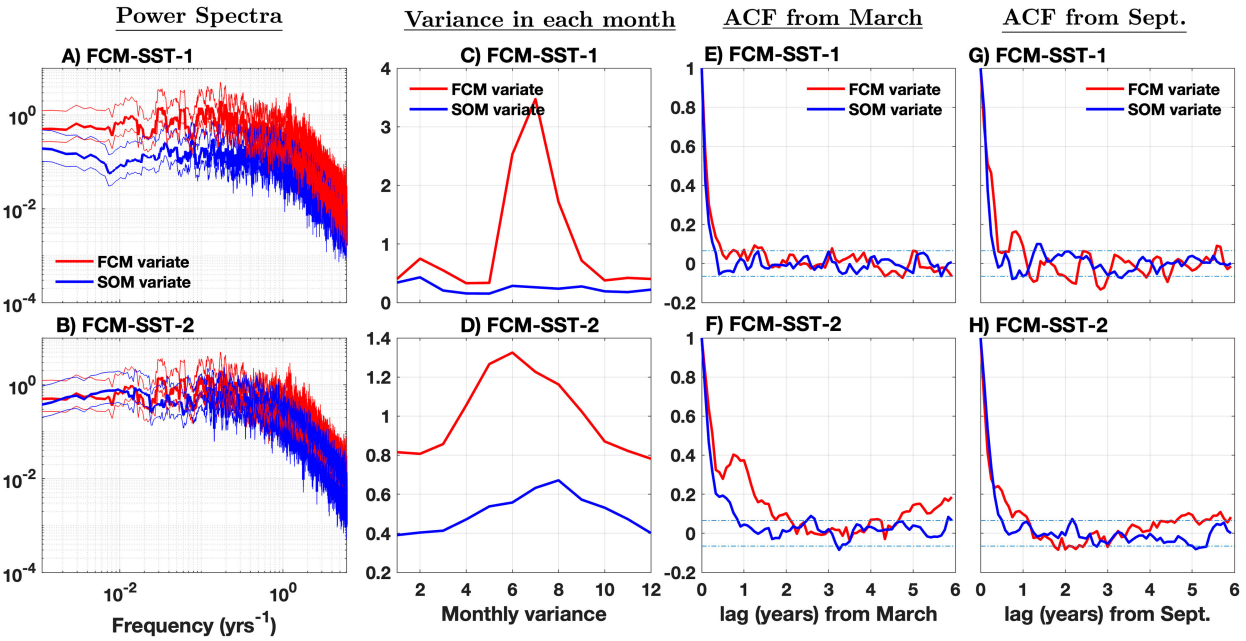


FIG. 9. Power spectra, variance distribution with month, and seasonal ACFs of the variate time series for the two modes with higher variance in the FCM (FCM-SST-1 and FCM-SST-2). Power spectra of the unnormalized SOM variate (blue) and FCM variate (red) for (a) FCM-SST-1 and (b) SOM-SST-2. The thick lines are the power spectral density and the thin lines are the 95% confidence interval of the power spectra. The variance of the unnormalized SOM variate (red) and FCM variate (blue) as a function of month for (c) FCM-SST-1 and (d) FCM-SST-2. Seasonal ACF from March of the SOM variate (blue) and FCM variate (red) for (e) FCM-SST-1 and (f) FCM-SST-2. Seasonal ACF from September of the SOM variate (blue) and FCM variate (red) for (g) FCM-SST-1 and (h) FCM-SST-2. The dash-dotted blue lines in (e)–(h) indicate the level of correlations that are significantly different from zero at the 95% confidence level.

Zhang et al. 2014), and these dynamics likely explain the weak Atlantic Niño mode found in the SOM.

Power spectra of the (unnormalized) SOM and FCM variates (Fig. 9a) demonstrate that the FCM variate has more variance than the SOM variate at all frequencies. The variance difference between the SOM and FCM is concentrated in the summer months (in July, the FCM variate has about 13 times more variance than the SOM variate), while the variance differences in other seasons are small (Fig. 9c). It is well known that Atlantic Niño peaks in the summertime (Zebiak 1993; Keenlyside and Latif 2007; Prodhomme et al. 2019). The persistence of the SOM and FCM variates is limited to a few months (Figs. 9e,g), in accord with the characteristic time scales of Atlantic Niño (Dippe et al. 2018).

It is widely accepted that the Atlantic Niño arises from mechanisms similar to the Pacific Niño, which includes a significant role for downwelling oceanic Kelvin waves and a Bjerknes feedback (see SLP signature in Fig. S4), both of which require interactive ocean dynamics (Xie and Carton 2004; Foltz and McPhaden 2010; Lübbecke and McPhaden 2017; Dippe et al. 2018; Silva et al. 2021). Atlantic Niño arises organically as a component containing more SST variance in the FCM, confirming that CDA can isolate the dynamical modes of SST variability related to ocean dynamics using only the raw SST fields.

A mode of SST variability that is concentrated in the subpolar North Atlantic emerges as the component with the second most extreme enhancement of SST variance in the FCM (FCM-SST-2). SST variance differences are concentrated in the region east of the Grand Banks (termed the subtropical–subpolar "transition zone"; see Buckley and Marshall 2016) with smaller magnitude anomalies of the opposite sign in the central subpolar gyre (Figs. 10b,c; pattern correlation over CDA domain is 0.97). The ST anomalies are about 30% weaker in the SOM, as $\sqrt{\lambda_{29}} = 0.7$. It is worth mentioning that the precise pattern and significance of FCM-SST-2 depend somewhat on the EOF truncation used (Fig. A1), but regardless of the EOF truncation, we see that the variance differences are concentrated in the subpolar North Atlantic. The fact that we find modes of SST variability in the subpolar North Atlantic that have more variance in the FCM than in the SOM is in line with previous studies that suggest the importance of ocean dynamics in setting SST in subpolar regions (Buckley et al. 2014, 2015; Buckley and Marshall 2016; Piecuch et al. 2017; Delworth et al. 2017; Wills et al. 2019).

Power spectra of the (unnormalized) SOM and FCM variates (Fig. 9b) demonstrate that the FCM has more variance than the SOM at all frequencies, although there is significant overlap between the spectra. The variance ratio does not differ substantially with season, and both the FCM and SOM variates have maximum variance in the summertime (Fig. 9d). The seasonal ACF of the FCM variate starting in March shows an initial decay followed by an increase about 1 year later (Fig. 5f), which suggests that reemergence enhances the persistence of the FCM-SST-2 component in the FCM. Both

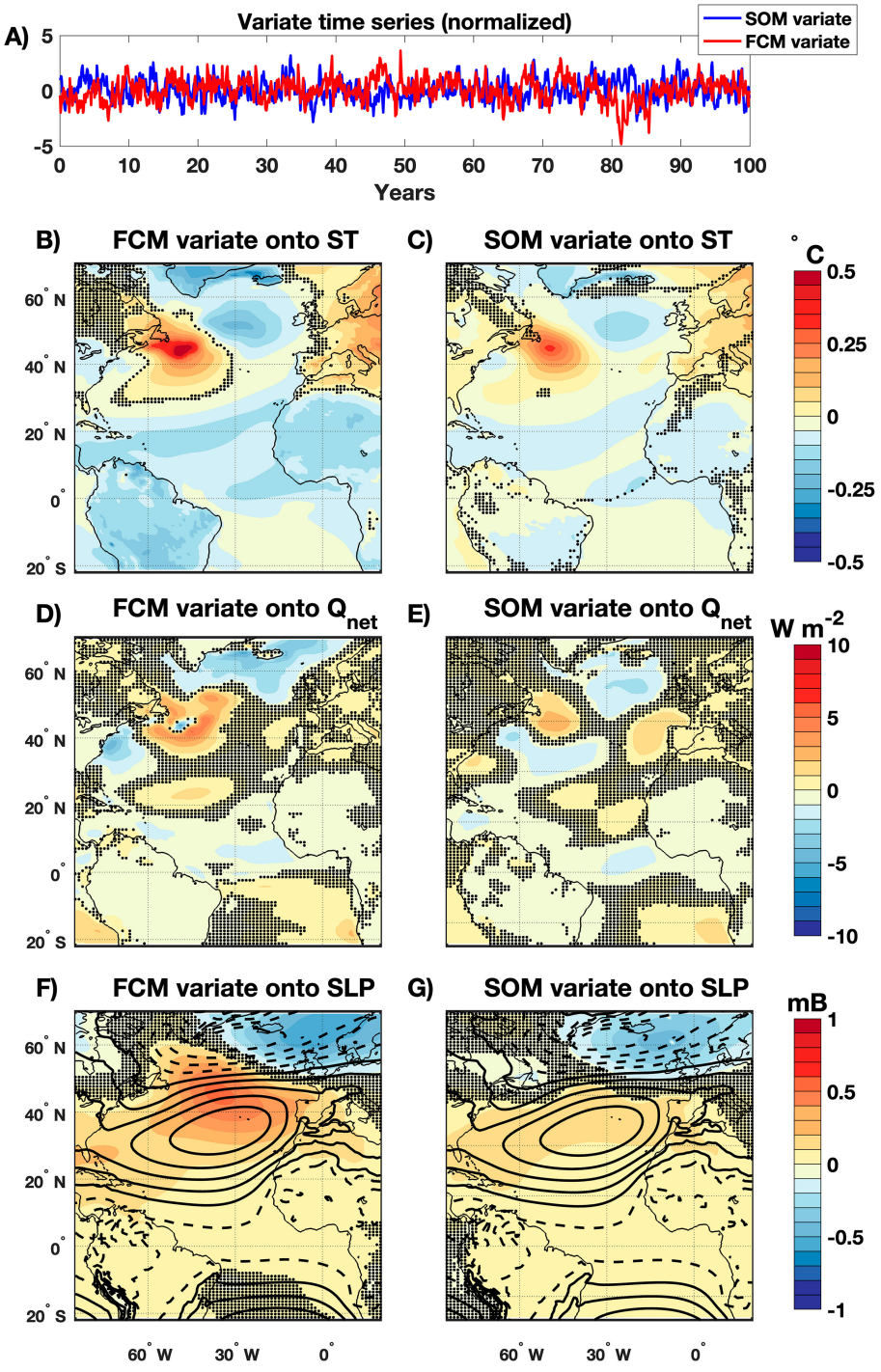


FIG. 10. The second leading component with enhanced SST variance in the FCM (FCM-SST-2; Fig. 3a). (a) A 100-yr sample of the normalized FCM variate (red) and SOM variate (blue). Regression slope between the FCM variate time series and (b) FCM ST, (d) FCM $Q_{net}$, and (f) FCM SLP. Regression slope between the SOM variate time series and (c) SOM ST, (e) SOM $Q_{net}$, and (g) SOM SLP. In (b)–(g), the black dots show grid points where the regression is not significant at the 95% confidence level. Regressions are computed with $Q_{net}$ 1 month prior to the variate time series. Positive $Q_{net}$ means ocean gains heat from atmosphere. In (f) and (g), the mean SLP field is shown in black contours with a contour interval of 2 mb. The solid and dashed contours indicate the SLP values above and below the standard average pressure at sea level (1013.25 mb), respectively.

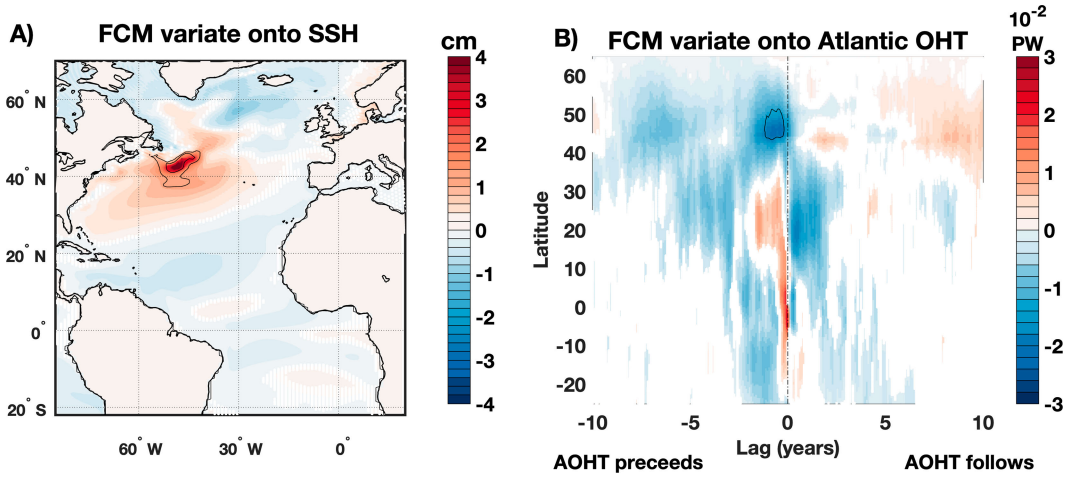


FIG. 11. Relationship between FCM-SST-2 (Figs. 3a and 10a,b) and ocean processes. (a) Regression of the FCM variate with SSH. Regression slope is shown in colors, and $R^2$ of the regression is shown in black contours, with contours at levels [0.1, 0.2, 0.3]. (b) Lagged correlation of the FCM variate and the AOHT as a function of latitude and lag. Negative (positive) lags imply that the AOHT precedes (follows) the variate time series. The regression slope is shown in colors, and $R^2$ is shown in the black contour; the contour is at a level of 0.05. In both panels, regressions that are not significant at the 95% confidence level are stippled white.

the seasonal ACF of the FCM variate from March (Fig. 5f) and September (Fig. 5h) show modest interannual persistence that appears unrelated to reemergence, while neither of the seasonal ACFs of the SOM variate show interannual persistence (Figs. 5f,h).

To gain insight into the mechanisms associated with component FCM-SST-2, we compute regression maps with selected oceanic and atmospheric variables (Figs. 10d–g and 11). In the SOM, $Q_{net}$ 1 month prior forces the SST anomalies, as must be the case since air–sea heat fluxes are the only mechanism for creating SST anomalies in the SOM (Figs. 10c,e). In contrast, in the FCM, the relationship between SST and $Q_{net}$ 1 month prior is not a simple forcing or damping, but rather $Q_{net}$ patterns that are shifted relative to the SST patterns (Figs. 10b,d). Anomalies in $Q_{net}$ damp the SST anomaly at the location of the maximum anomaly, but force SST anomalies downstream.

The SLP patterns associated with FCM-SST-2 (Figs. 10f,g) are significantly stronger in the FCM than in the SOM. Since the SOM and FCM differ only in their oceans, these SLP variance differences must originate from the SST or sea ice variance differences, specifically the stronger SST signature of this component in the FCM as compared to the SOM. Recent studies indicate that the atmosphere has a robust response to SST anomalies over western boundary current extensions (Wills et al. 2016; Bishop et al. 2017; Small et al. 2019), such as the Gulf Stream Extension/North Atlantic Current (where we see maximal SST anomalies in FCM-SST-2). Our results are also consistent with the negative NAO response resulting from cooling in the central subpolar Atlantic and warming along the Gulf Stream path seen by Karnauskas et al. (2021).

Differences between the SOM and FCM may be due to either one-dimensional mixed layer processes (e.g., seasonal variations in heat capacity and entrainment) or three-dimensional ocean dynamics (e.g., the AMOC and gyre circulations). Regression slopes between the FCM variate time series and the MLD are of small magnitude (maximum of 20 m; not shown) and explain very little of the MLD variance (maximum of less than 5% of the variance), suggesting that the role of interannual variations in the MLD is small. FCM-SST-2 is associated with positive sea surface height (SSH) anomalies in the western subtropical and subpolar gyres (Fig. 11a), consistent with a strengthened subtropical gyre, a weakened subpolar gyre, and an increased penetration of subtropical waters into the subpolar gyre, a mode of SSH variability that has been described previously (Häkkinen and Rhines 2004; Böning et al. 2006; Häkkinen and Rhines 2009; Häkkinen et al. 2011; Holliday et al. 2008, 2015; Piecuch et al. 2017; Desbruyères et al. 2021). The maximum SSH anomalies are located along the path of the North Atlantic Current, and in this region, the mode of variability locally explains about 30% of the monthly anomalies of SSH (Fig. 11a).

The Atlantic ocean heat transport (AOHT) signature associated with FCM-SST-2 is quite weak, with maxima on the order of a few hundredths of a petawatt, only a few percent of the annual mean AOHT, which has a maximum of about 1.2 PW in CESM1 (see Fig. 2 in Larson et al. 2020). The portion of the local AOHT variance that is explained by the FCM variate has a maximum of only 7%. However, the AOHT variations which precede the FCM variate leads to the convergence of heat between 35° and 50°N, consistent with the positive SST anomalies in the Grand Banks region. The divergence of AOHT north of 50°N is consistent with the weaker negative SST anomalies found in the central and eastern subpolar gyre north of 50°N. A back of the envelope calculation suggests that an AOHT convergence of 0.03 PW sustained over 2 years could change the temperature by 0.5°C if the convergence occurs in a relatively small region (10° latitude and 20° longitude and over the top 500 m). However, a formal heat budget would be

required to quantitatively determine the role of AOHT in the SST anomalies associated with FCM-SST-2.

### d. Relationship between CDA components and the AMV

The AMV index, defined as SST anomalies averaged over the North Atlantic basin from 0° to 60°N, is significantly stronger in the SOM than in the FCM; the variance of the AMV index in SOM divided by variance of the AMV index in the FCM is 2.2. The spatial patterns of the AMV in the SOM (Fig. 6e) and in the FCM (Fig. 6f) show a characteristic horseshoe structure, and the amplitude of AMV-related SST anomalies in the subpolar North Atlantic is stronger in the SOM than in the FCM. The fact that the AMV mode has more variance in the SOM than in the FCM confirms ocean dynamics are not necessary for the AMV, in line with Clement et al. (2015), and interactive ocean dynamics damps the AMV.

As mentioned earlier, the ST regression patterns associated with SOM-SST-2 resemble the AMV. For SOM-SST-2, the correlation coefficient between the SOM variate time series and the SOM AMV index is $\rho = 0.76$ (Fig. 6a); the correlation between the FCM variate time series and the FCM AMV index is weaker, with a correlation $\rho = 0.62$ (Fig. 6b). The coherence between SOM-SST-2 variates and the AMV index is strongest at low frequencies for both the SOM variate and the FCM variate (Fig. S5). The AMV index in the SOM is also correlated with the SOM variate of SOM-SST-1 (correlation of 0.33 when SOM variate precedes the AMV by 2 months, see Fig. S5a) and to a lesser extent the SOM variate of SOM-SST-3 (correlation of 0.29 of when SOM variate precedes the AMV by 1 month; see Fig. S5a). The strong coherence between the SOM-SST-1 SOM variate and the SOM AMV at low frequencies (max $\rho \approx 0.85$ occurs at a time scale of approximate 50 years; see Fig. S5a) suggests that the NAO tripole strongly projects onto the AMV at low frequencies. It is not surprising that large-scale atmospherically forced modes of variability project strongly onto a basinwide index such as the AMV, particularly in the SOM where SST variability can only be due to stochastic atmospheric forcing.

In the FCM, FCM-SST-2, the subpolar mode of SST variability, is also correlated with the AMV (correlation of $-0.31$ when the FCM variate follows the AMV by 1 month; see Fig. S5c). The importance of subpolar SST anomalies for low-frequency AMV variability has been noted previously (Zhang and Zhang 2015; Zhang 2017; Kim et al. 2019; Yan et al. 2019; Li et al. 2020). Some studies have suggested alternative AMV indices that specifically isolate SST variability in the subpolar gyre (Yan et al. 2019; Wills et al. 2019). For example, Wills et al. (2019) calculate an AMV index based on low-frequency component analysis and find that the SST anomalies associated with this index are restricted to subpolar regions.

While the distribution of AMV-related SST variance among multiple CDA components may make it more difficult to relate our analysis to prior literature on AMV mechanisms, recent work has shown that basinwide SST variability is set by a mix of different processes that are important on different time scales and in different regions (Vecchi et al. 2017; Li et al. 2020). Our analysis confirms that basinwide SST variability is set by a mix of processes, and the specific mix of processes differs between the SOM and FCM. In the SOM, the AMV is set by several atmospherically forced modes of SST variability, including a tripole-like mode (SOM-SST-1) and a horseshoe-like pattern (SOM-SST-2). The AMV in the FCM is also related to a atmospherically forced mode with canonical horseshoe structure (SOM-SST-2), but a subpolar mode with elevated variance in the FCM (FCM-SST-2) also influences the basinwide SST. This CDA component captures the role of ocean dynamics in enhancing AMV variance.

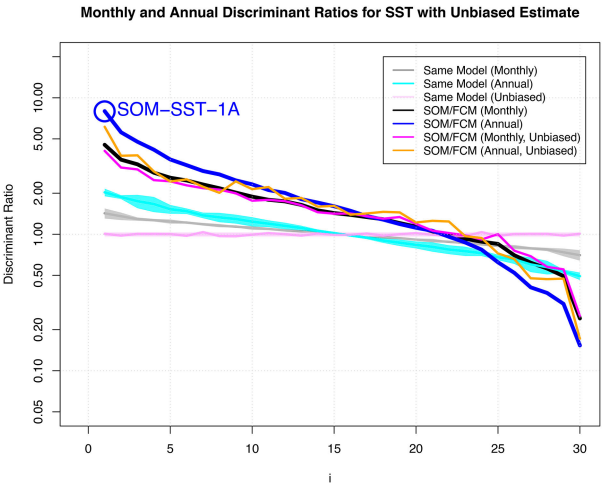


FIG. 12. A comparison of CDA analyses based on annual mean SST and monthly (deseasonalized) SST (both cases use a 30-EOF truncation). The discriminant ratios as a function of discriminant order [Eq. (6)] for the monthly and the annual CDA analysis are shown in the black and blue lines, respectively. The null hypotheses of equal variability using two halves from the same model for the monthly and annual CDA analysis are shown by the gray and cyan lines, respectively (thick line is the mean and the shading shows the range of two standard deviations). The unbiased discriminant ratios [Eq. (11)] for the monthly and annual CDA analysis are shown by the pink and orange lines, respectively.

## 5. Sensitivity analysis: Role of ocean dynamics in annual SST differences

Since CDA maximizes variance ratios, the results of CDA may depend on the frequency of the output analyzed. In this section, we apply CDA to annual average Atlantic SST in the FCM and SOM and compare to our results from CDA analysis using monthly (deseasonalized) SST. We use the same EOF truncation for our annual CDA analysis. The discriminant ratios (Fig. 12) demonstrate that Atlantic SST variability in the SOM and FCM are significantly different. As for the monthly CDA analysis, there are more components where the SOM has significantly larger variance ($\lambda_i > 1$) than components where the FCM has more variance ($\lambda_i < 1$). The variance ratios for the annual CDA analysis (blue line in Fig. 12) are significantly larger than those from the monthly CDA analysis (black line in Fig. 12).

Because annual averaging reduces the degrees of freedom, overfitting is a concern. To assess overfitting, we compute

unbiased estimates of the discriminant ratios $\lambda_{iu}$, in which one-half of the data is used for finding $\mathbf{q}_i$ and the other half is used for calculating the discriminant ratio [see Eqs. (10) and (11)]. For the yearly CDA analysis, the $\lambda_{iu}$ (orange line in Fig. 12) are generally smaller than the $\lambda_i$ (blue line in Fig. 12), implying that the larger variance ratios found for the annual CDA analysis are due to overfitting. For the monthly CDA analysis, the $\lambda_{iu}$ (pink line in Fig. 12) and the $\lambda_i$ (black line in Fig. 12) are nearly identical, suggesting that overfitting does not affect the monthly CDA analysis. Furthermore, the $\lambda_{iu}$ from the yearly analysis (orange line) and the $\lambda_i$ from the monthly analysis (black lines) are very similar, confirming that after we account for overfitting, discriminant ratios are not dependent on the frequency of the output analyzed.

The components isolated from our annual CDA analysis are quite similar to those isolated from our monthly CDA analysis. The component with the most extreme enhancement of variance in the FCM remains a tropical mode that is highly correlated with Atlantic Niño; the correlation of the FCM variate with the FCM Atlantic Niño index is 0.83, and the correlation of the SOM variate with the SOM Atlantic Niño index is 0.46.

The component with the most extreme enhancement of variance in the SOM (SOM-SST-1A) is tripolar in structure (Figs. 13c,d), similar to the leading component with more variance in the SOM from the monthly CDA SST analysis (SOM-SST-1; Fig. 4). However, the subtropical anomalies for SOM-SST-1A are somewhat weaker than for SOM-SST-1, and thus, SOM-SST-1A projects more strongly onto the AMV than SOM-SST-1 (although not as strongly as SOM-SST-2). For SOM-SST-1A, the correlation of the SOM variate with the SOM AMV index is 0.66 and the correlation of the FCM variate with the FCM AMV index is 0.36 (Figs. 13a,b). In the SOM, $Q_{\text{net}}$ anomalies force ST anomalies associated with SOM-SST-1A (Figs. 13c,e), as they must since there is no other means for creating ST anomalies. In the FCM, the relationship between anomalies of ST and $Q_{\text{net}}$ is more complex (Figs. 13d,f). The regions of maximum $Q_{\text{net}}$ anomalies are somewhat displaced from the regions of maximal SST anomalies, and in a few regions (e.g., the West Greenland and Labrador Currents), $Q_{\text{net}}$ damps the ST anomalies.

The mode with the second most extreme enhancement of variance in the SOM resembles SOM-SST-3, and this component does not exhibit a strong relationship with the AMV. These results suggest that for annual and longer time scales, the NAO tripole and the AMV are not distinguishable in our statistical analysis. A possible hypothesis is that the AMV is simply the longer time-scale response to the NAO. Tropical processes, such as wind–evaporation feedback, may enhance the persistence of NAO-related SST anomalies in the tropics, while processes such as reemergence may enhance NAO-related SST anomalies in the subpolar gyre. Enhanced persistence of SST anomalies in the tropics and subpolar gyre, without such enhanced persistence in the subtropics, may lead the NAO tripole to decay into a horseshoe-shaped structure, which is the canonical AMV pattern.

## 6. Do SST differences lead to atmospheric differences?

The SOM and FCM have exactly the same dynamics, except that the SOM has no interactive ocean dynamics. Therefore, the cause of any model differences, even in the atmosphere, is due to interactive ocean dynamics. A natural question is what is the impact of changing ocean dynamics on the atmosphere? To answer this question, we apply CDA to SLP in the Atlantic region to test equality of atmospheric variability between the SOM and FCM. For this analysis, we consider monthly (deseasonalized) SLP. The resulting discriminant ratios for SLP (Fig. 14a) are much closer to one than those for SST, but the most extreme discriminant ratios are statistically significant (SOM-SLP-1 and FCM-SLP-1; Fig. 14a).

Analysis of divergence reveals that the leading component with the most extreme enhancement of SLP variance in the SOM (SOM-SLP-1) is primarily due to differences in the mean SLP (Fig. 14b). In contrast, the leading component with the most extreme enhancement of SLP variance in the FCM (FCM-SLP-1) is primarily due to differences in internal SLP variability between the SOM and FCM (Fig. 14b). SOM-SLP-1 describes 45.5% of the total divergence, and FCM-SLP-1 describes 16.5%; together, these two components describe 62% of the total SLP divergence.

The SLP differences between the FCM and the SOM are clearly related to SST and/or sea ice differences, but the components isolated from the SLP analysis are a mixture of the SST CDA components. The spatial patterns of SLP and ST associated with FCM-SLP-1 (Figs. 15c–f) resemble those of Atlantic-Niño/FCM-SST-1 (Figs. 8c,d and Fig. S4) in the tropical Atlantic. However, the midlatitude ST and SLP structures of FCM-SLP-1 differ substantially from those of FCM-SST-1 (cf. Figs. 15c–f to Figs. 8c,d and Fig. S4). The ST signatures over land are more substantial, and the SLP anomalies over the midlatitudes are much larger for FCM-SLP-1 than FCM-SST-1. Despite a meridional dipole structure in SLP, FCM-SLP-1 is not strongly correlated with the NAO (Fig. S1b) in either the SOM ($\rho = 0.11$) or the FCM ($\rho = 0.13$).

In the North Atlantic, the spatial patterns of SLP associated with SOM-SLP-1 are dipolar in structure (Figs. 16b,c), and the ST patterns exhibit tripolar structures (Figs. 16d,e). The importance of the differences in mean to the divergence of SOM-SLP-1 suggests that the mean ST bias between the SOM and the FCM is important to explain the structure of SOM-SLP-1. Additionally, SST variance differences associated with SOM-SST-1, SOM-SST-2, and SOM-SST-3 explain a total of 50% of the variance of SOM-SLP-1 for the SOM and 26% of the variance of SOM-SLP-1 for the FCM.

## 7. Can memory differences fully explain SST differences between the SOM and FCM?

It is possible that the difference between the SOM and FCM can be explained simply as a difference in memory time scale. To investigate this possibility, we regress out SST 1 month prior from each row of $\mathbf{F}_s$ and $\mathbf{F}_c$ [Eq. (2)] and perform CDA on the residuals. Regressing out SST information from 1 month prior removes both memory and potentially

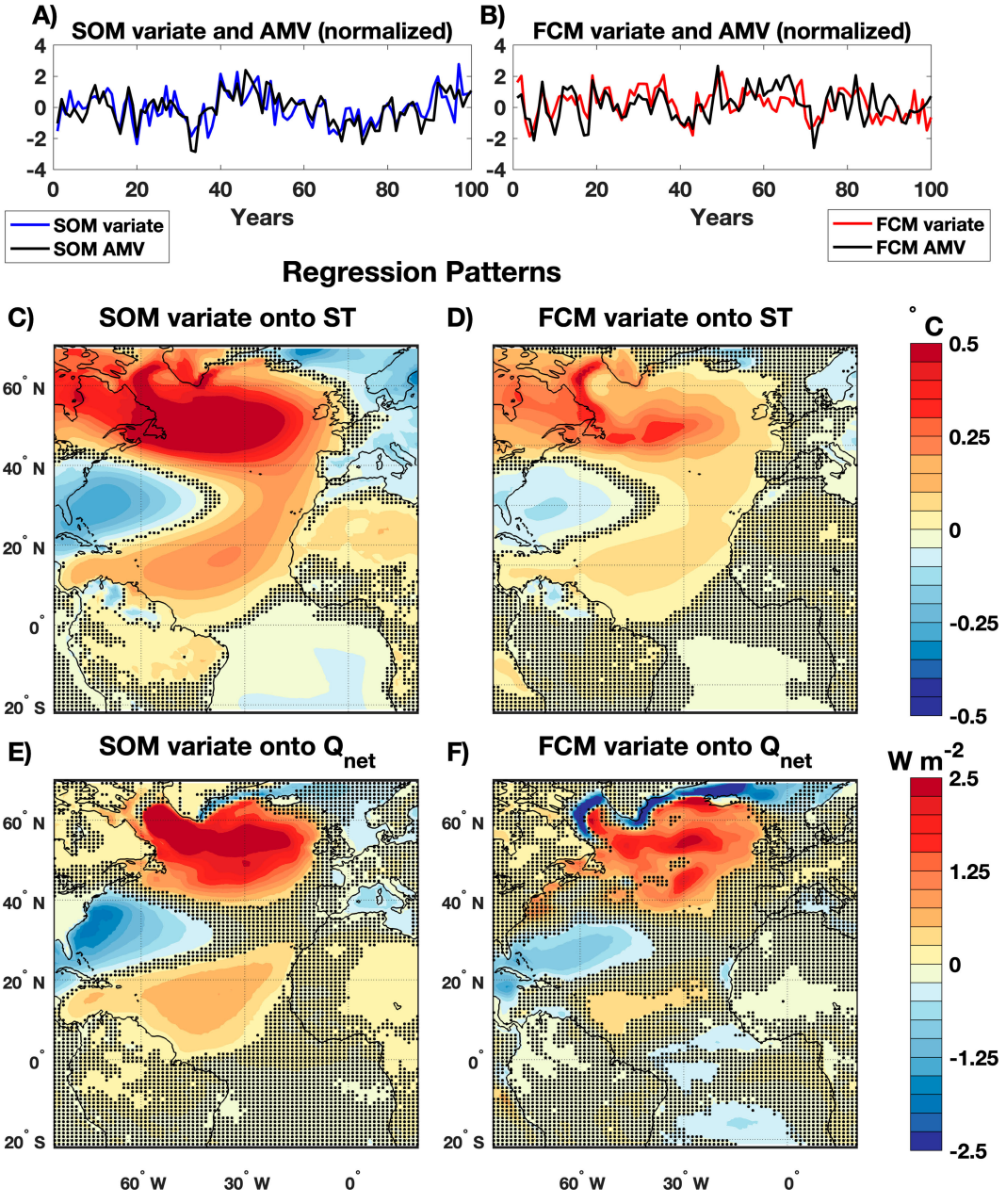


FIG. 13. CDA analysis of annual SST data: the leading component with enhanced SST variance in the SOM (SOM-SST-1A in Fig. 12). (a) A 100-yr sample of the normalized SOM variate (blue) and the normalized SOM AMV (black). The correlation of the SOM variate and the SOM AMV is 0.66. (b) 100-yr sample of the normalized FCM variate (red) and the normalized FCM AMV (black). The correlation of the FCM variate and the FCM AMV is 0.36. The regression slope between the normalized SOM variate and (c) ST and (e) $Q_{net}$. The regression slope between the normalized FCM variate and (d) ST and (f) $Q_{net}$. The dots in (c)–(f) show where the regression is not significant at the 95% confidence level. Regressions with $Q_{net}$ in (e) and (f) are computed with $Q_{net}$ 1 year prior to the variate time series.

active ocean dynamics, which are captured within the lagged relationships between the principal component time series used to comprise $\mathbf{F}_s$ and $\mathbf{F}_c$. We find that regressing out SST 1 month prior reduces the SST variance differences between the SOM and FCM (cf. Fig. 17a, gray and black lines). More variance is removed from the SOM than from the FCM (discriminant ratios shift downward), making them more symmetrical about $\lambda_i = 1$.

We utilize the resulting discriminant ratios from each analysis to calculate total divergence values (Fig. 17b); only total divergences due to internal variability [$\mathscr{D}_v$, Eq. (15)] are considered because the residuals have zero mean. If

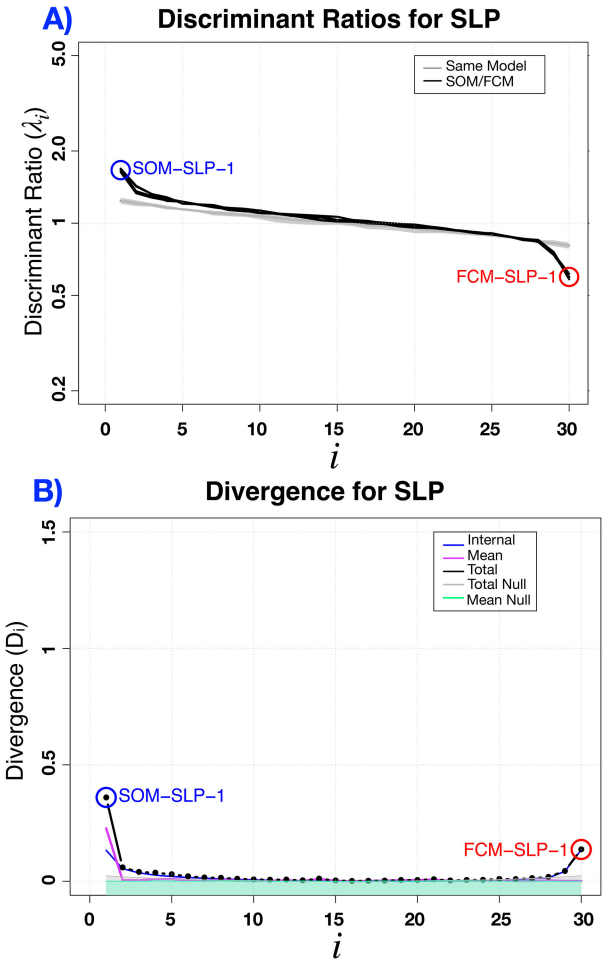


FIG. 14. CDA analysis comparing monthly (deseasonalized) Atlantic SLP variance in the FCM and SOM. (a) Discriminant ratios as a function of the discriminant order for a 30-EOF truncation [Eq. (6)]. The black lines show the leading discriminant ratios when the variance ratio of the SOM/FCM is maximized. The gray line shows the null hypothesis of equal variability using two halves from the same model and the gray shading shows the range of two standard deviations. (b) Divergence representative of the discriminant ratios. The black line shows the divergence ($D_i$), the purple line shows the divergence due to the difference in means ($D_{m_i}$), and the blue line shows the divergence due to differences in internal variability ($D_{v_i}$). The gray shading is the null hypothesis for divergence, and the green shading denotes the null hypothesis line for the divergence due to the mean; both null cases are calculated using two halves from the same model.

$\mathscr{D}_v$ has a value that overlaps with the 95% confidence interval from the null hypothesis (Fig. 17, gray shading), the models are said to have indistinguishable internal variability. We find that the original case has a divergence value of about 8. After we regress out SST 1 month prior, $\mathscr{D}_v$ reduces to about 5.5, but this value is well outside the interval for the null hypothesis. Therefore, we conclude that differences in variability between the SOM and the FCM remain statistically significant.

We now investigate whether regressing out SST beyond 1 month prior further reduces variance differences between the SOM and the FCM. We sequentially regress out SST between 1 and $\tau_M$ months prior, where $\tau_M$ ranges from 2 to 84 months. Then, we calculate CDA on the residuals. This results in 84 separate CDA analyses with distinct discriminant ratios. For lags beyond 1 month, $\mathscr{D}_v$ is nearly independent of $\tau_M$ (Fig. 17b, yellow shading), implying that regressing out SST at lags longer than 1 month does not reduce $\mathscr{D}_v$. This result might be surprising because the ocean memory is longer than 1 month, but this memory is likely captured in the lagged relationship between the principal component time series used to comprise $\mathbf{F}_s$ and $\mathbf{F}_c$. Importantly, $\mathscr{D}_v$ remains highly significant in comparison to the null hypothesis, indicating that SST in the CESM1 SOM and FCM are statistically different even when we crudely account for differences in memory. However, given the strong seasonal dependence of the differences between the SOM and the FCM, a more sophisticated regression accounting for seasonal memory differences may be able to explain more of the variance differences between the SOM and the FCM.

## 8. Conclusions

This paper investigates the role of interactive ocean dynamics in Atlantic SST variability. The approach is to compare SST variability in a fully coupled atmosphere–ocean–ice model (FCM) to an atmosphere–ice model coupled to a motionless slab ocean (SOM) with a depth set to the spatially varying annual mean climatological mixed layer depth. The FCM has more SST variance than the SOM in the tropics (Fig. 2), where active ocean dynamics leads to elevated SST variance. The SOM has higher variance than the FCM in the extratropics (Fig. 2) due to the lack of oceanic damping, primarily entrainment damping, in the SOM (G. Liu et al. 2023).

Differences in SST variability between the two models are diagnosed by finding components whose variance differs as much as possible between the two models using covariance discriminant analysis (CDA; DelSole and Tippett 2022). This optimization technique reveals numerous differences between the two models, indicating that interactive ocean dynamics impacts Atlantic SST variability in a way that is statistically distinguishable (Fig. 3a). Analysis of the divergence demonstrates that SST differences between the SOM and FCM are mainly due to differences in SST variance rather than the mean SST (Fig. 3b).

The component with the most extreme enhancement of SST variance in the SOM (SOM-SST-1) resembles the tripole SST pattern associated with the NAO (Fig. 4). A mode of SST variability with a horseshoe structure that resembles the AMV emerges as a component with the second most extreme enhancement of SST variance in the SOM (SOM-SST-2; Fig. 6). The component with the third most enhancement of variance in the SOM (SOM-SST-3) is also tripolar, but the tripole is shifted northward compared to SOM-SST-1 (Fig. 7).

Components with more variance in the SOM have several common features. These components are excited by stochastic atmospheric forcing, as they must be as there is no other forcing

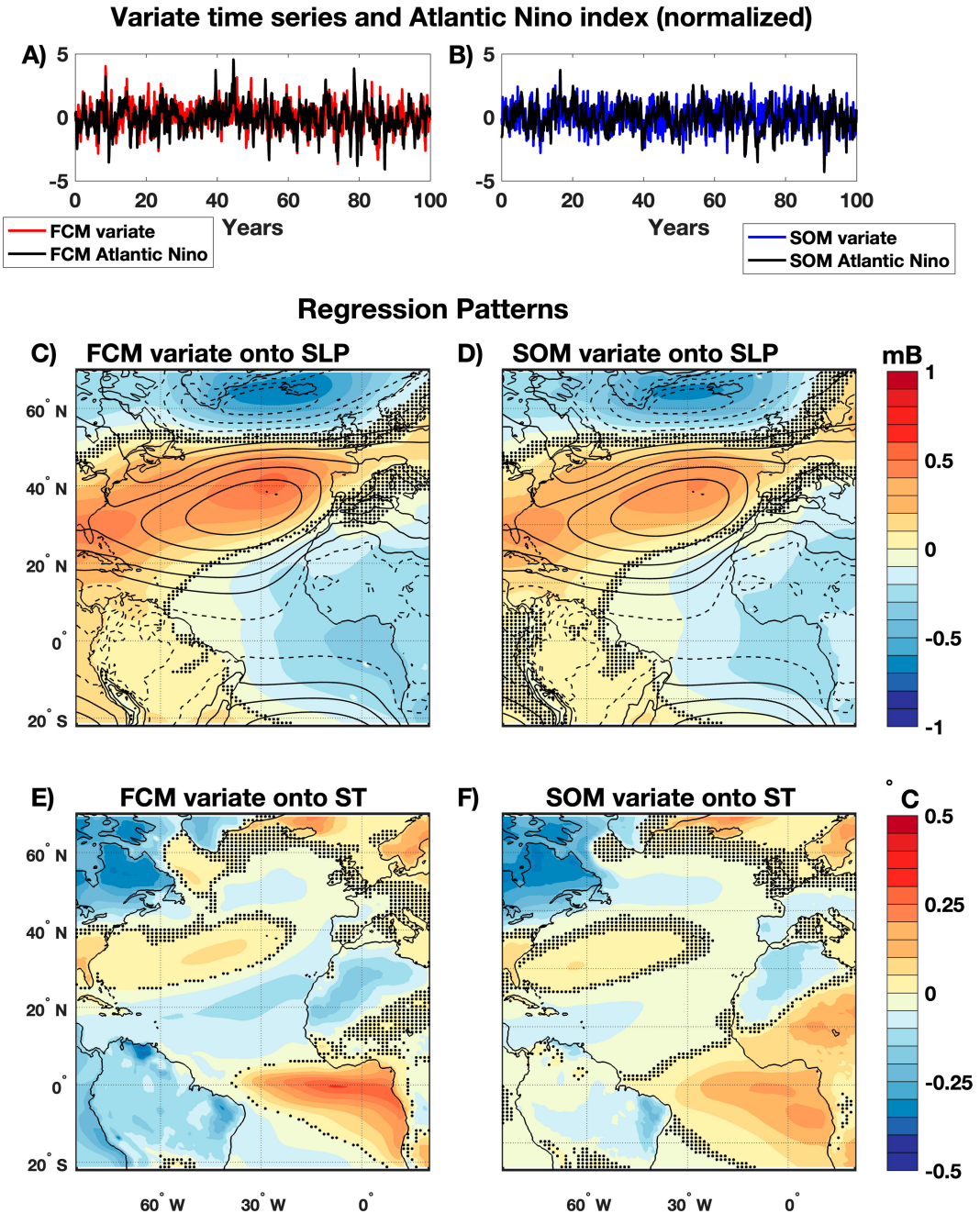


FIG. 15. The leading component with enhanced SLP variance in the FCM (FCM-SLP-1; Fig. 14a). (a) A 100-yr sample of the normalized FCM variate (red) and the normalized FCM Atlantic Niño index (black). The FCM variate and the FCM Atlantic Niño index have a correlation coefficient of $\rho = 0.55$. (b) A 100-yr sample of the normalized SOM variate (blue) and the normalized SOM Atlantic Niño index (black). The SOM variate and the SOM Atlantic Niño index have a correlation coefficient of $\rho = 0.46$. The regression slope between the normalized FCM variate and (c) SLP and (e) ST. The regression slope between the normalized SOM variate and (d) SLP and (f) ST. The dots in (c)–(f) show where the regression is not significant at the 95% confidence level. In (c) and (d), the mean SLP field is shown in black contours with a contour interval of 2 mb. The solid and dashed contours indicate SLP values above and below the standard average pressure at sea level (1013.25 mb), respectively.

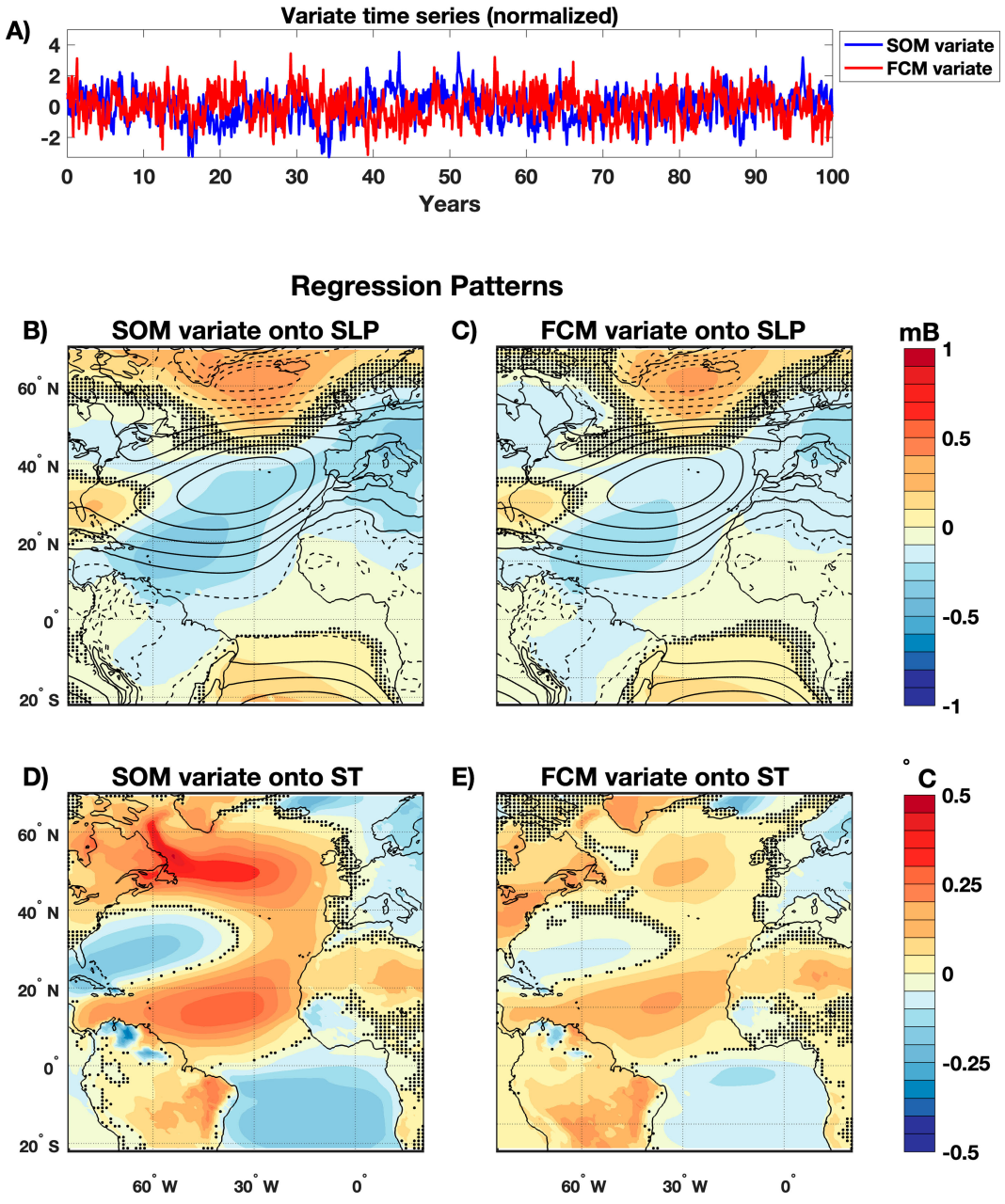


FIG. 16. The leading component with enhanced SLP variance in the SOM (SOM-SLP-1; Fig. 14a). (a) A 100-yr sample of the normalized FCM variate (red) and the normalized SOM variate (blue). The regression slope between the normalized SOM variate and (b) SLP and (d) ST. The regression slope between the normalized FCM variate and (c) SLP and (e) ST. The dots in (b)–(e) show where the regression is not significant at the 95% confidence level. In (b) and (c), the mean SLP field is shown in black contours with a contour interval of 2 mb. The solid and dashed contours indicate SLP values above and below the standard average pressure at sea level (1013.25 mb), respectively.

mechanism in the SOM. The atmospheric forcing associated with these components is the same amplitude in the SOM and the FCM (Figs. 4d,e and 7d,e and Fig. S3), but the ocean response to this forcing is weaker in the FCM.

The differing response of the ocean to atmospheric forcing is primarily explained by seasonal mixed layer depth variations, which are present in the FCM but not in the SOM. Air–sea heat fluxes are stronger in winter than in summer in both the SOM and the FCM (Fig. S2); in the SOM, SST variations are also larger in wintertime. In the FCM, seasonal variations in the mixed layer depth act to reduce SST variance in wintertime. Air–sea heat fluxes are less efficient at changing SST when the mixed layer is deeper. Furthermore, entrainment damps SST anomalies in fall/winter as the mixed layer deepens, reducing

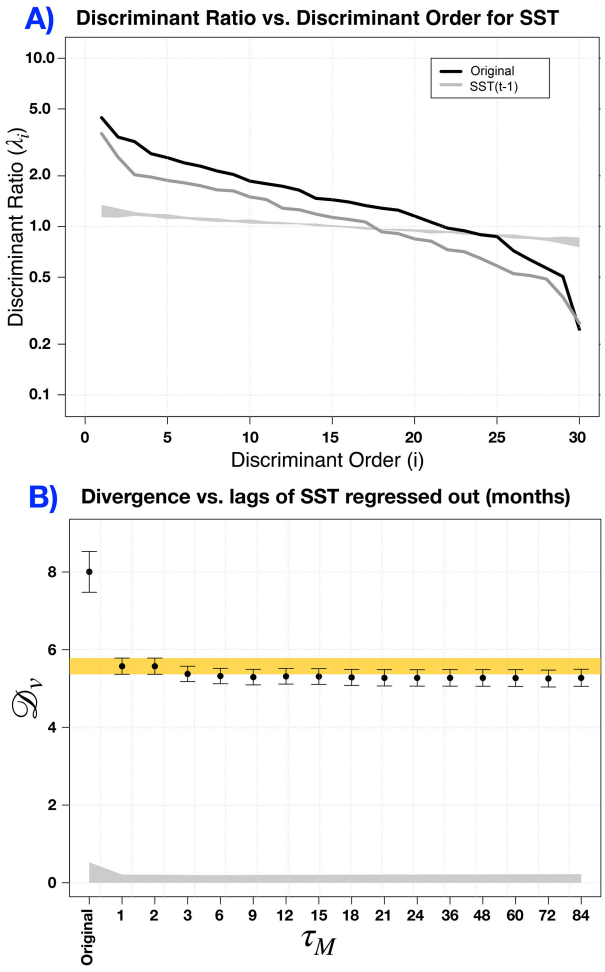


FIG. 17. Results comparing SST CDA with and without regressing out ocean memory. (a) Discriminant ratio for original CDA analysis (black line) (same as Fig. 3a) and CDA computed when SST 1 month prior is regressed out (gray line). The gray shading shows the range of two standard deviations in the null hypothesis of equal variability using two halves from the same model with SST 1 month prior regressed out. (b) Total divergence of original CDA analysis and CDA analysis when we sequentially regress out SST between 1 and $\tau_M$ months prior, where $\tau_M$ ranges from 1 to 84 months. The gray shading denotes $\mathscr{D}_v$ for the null hypothesis of equal variance. The yellow shading indicates the range of the divergence when SST 1 month prior is regressed out.

the wintertime SST variance in the FCM. As a result, components with more variance in the SOM (e.g., SOM-SST-1, SOM-SST-2, and SOM-SST-3) show strongly elevated SST variance in the SOM in wintertime and a much more muted seasonal distribution of SST variance in the FCM (Figs. 5d–f).

Seasonal variations in mixed layer depth also act to increase the memory in wintertime. The higher heat capacity of the mixed layer in winter leads to higher persistence in this season. Additionally, SST anomalies formed during wintertime can be isolated beneath the seasonal thermocline in summer and reemerge the following winter when the mixed layer deepens. For components with higher variance in the SOM, the SOM exhibits high summer persistence as the weak summertime stochastic atmospheric forcing is distributed over the relatively deep slab layer (set to be the annual mean mixed layer depth). In contrast, in the FCM, there is a rapid loss of memory as the mixed layer shallows in summer (Figs. 5g–i). The NAO tripole–like component (SOM-SST-1) shows enhanced interannual persistence related to reemergence (Fig. 5g); a role for reemergence of the persistence of the NAO tripole was previously described in de Coëtlogon and Frankignoul (2003).

While components with more variance in the SOM have more variance at all frequencies, including low frequencies (Figs. 5a–c), the interannual memory is slightly longer in the FCM. This enhanced memory is seasonally dependent, with enhanced memory in winter (Figs. 5g–l). For SOM-SST-1 and SOM-SST-3, enhanced interannual memory in winter is related to the reemergence of SST anomalies (Figs. 5g,i). For the AMV-like component (SOM-SST-2), enhanced interannual memory in winter (Fig. 5h) does not appear related to reemergence, but rather to other oceanographic processes, such as variations in the three-dimensional ocean circulation (Zhang et al. 2016; O'Reilly et al. 2016; Delworth et al. 2017; Li et al. 2020; Oelsmann et al. 2020).

The leading component that has the most extreme enhancement of SST variance in the FCM (FCM-SST-1) is strongly related to Atlantic Niño (Fig. 8). The Atlantic Niño–like mode has significantly more variance in the summertime in the FCM, in accord with the previously described peak of Atlantic Niño peaks in the summertime (Zebiak 1993; Keenlyside and Latif 2007; Prodhomme et al. 2019), whereas the weak variability in the SOM has little seasonal dependence (Fig. 9c). Atlantic Niño arises organically as a component containing more SST variance in the FCM, confirming that CDA is a powerful tool that can isolate dynamical modes of SST variability related to ocean dynamics with only using the raw SST fields.

Strong subpolar SST anomalies in the subtropical–subpolar transition zone (Buckley and Marshall 2016) emerge as the second leading component with enhanced SST variance in the FCM (FCM-SST-2; Fig. 10). This finding supports previous studies that suggest the importance of ocean dynamics in setting SST in the subpolar North Atlantic (Buckley et al. 2014, 2015; Buckley and Marshall 2016; Piecuch et al. 2017; Delworth et al. 2017; Wills et al. 2019). Reemergence of SST anomalies is one mechanism that enhances the variance and the persistence of this component in the FCM (Fig. 9f). Three-dimensional ocean processes also likely play a role; modest Atlantic OHT variations are associated with this component, and these OHT variations are of the correct sign to force or enhance the SST anomalies associated with this mode (Fig. 11b).

The AMV in the SOM has about twice as much variance as the AMV in the FCM, supporting previous claims that the AMV is primarily explained by the low-frequency response to stochastic atmospheric forcing (Clement et al. 2015; Cane et al. 2017) and oceanic damping reduces the amplitude of the AMV (Murphy et al. 2021). The AMV is most related to a component with a canonical horseshoe structure (SOM-SST-2) in both the SOM and the FCM, but other components isolated from CDA are also correlated with the AMV. In the SOM, the

AMV is also related to tripolar SST anomalies associated with NAO-like atmospheric variability (SOM-SST-1), particularly at low frequencies. In the FCM, a subpolar mode with more variance in the FCM (FCM-SST-2) is also related to the AMV. Our analysis confirms that basinwide SST variability is set by a mix of processes that are important on different time scales and different regions (Vecchi et al. 2017; Li et al. 2020), and the specific mix of processes differs between the SOM and FCM. Thus, while our analysis is broadly consistent with previous claims that the AMV is primarily explained by the low-frequency response to stochastic atmospheric forcing (Clement et al. 2015; Cane et al. 2017), it is also consistent with the role of ocean dynamics in influencing SST in the subpolar North Atlantic (Buckley et al. 2014, 2015; Buckley and Marshall 2016; Piecuch et al. 2017; Delworth et al. 2017; Wills et al. 2019).

Despite large differences in SST between the SOM and the FCM, the atmospheres of the SOM and the FCM are quite similar. A CDA analysis of SLP finds that only two significance components explain the SLP differences between the SOM and the FCM (Fig. 14a). The component with more variance in the SOM is dominated by differences in the mean SLP, whereas the component with more variance in the FCM is dominated by differences in SLP variance (Fig. 14b).

After identifying leading dynamical components of SST differences between the SOM and FCM, we explore if the difference in memory can fully explain SST differences between the SOM and FCM. We find that a significant portion of variance differences between the SOM and FCM can be explained by regressing out SST 1 month prior. However, the models continue to have significant variance differences (Fig. 17). Given the strong seasonal dependence of the differences between the SOM and the FCM, a more sophisticated regression accounting for seasonal memory differences may be able to explain more of the variance differences between the SOM and the FCM.

Overall, we find that stochastic atmospheric forcing is able to explain the modes of basinwide Atlantic SST variability, including the NAO tripole SST anomalies and AMV-like SST anomalies, and ocean dynamics damps the variance of these stochastically generated modes. Interactive ocean dynamics enhances SST variance in the tropical Atlantic and to a lesser extent in the subpolar North Atlantic.

Our results suggest that some of the largest differences between the SOM and the FCM are due to the lack of one-dimensional mixed layer dynamics in the SOM, specifically entrainment damping and the seasonal variations in heat capacity of the mixed layer. The lack of these important, seasonally dependent one-dimensional processes in the SOM implies that while the stronger SST variance found in the SOM is sometimes closer to observations [as argued by Murphy et al. (2021) regarding low-frequency AMV variance], the elevated SST variance in the SOM is for the wrong reasons. The importance of one-dimensional mixed layer processes in the SST variance differences between the SOM and FCM suggests that, in order to isolate the contributions of three-dimensional ocean dynamics, we need a more complete model hierarchy, including an entraining mixed layer model.

Our results focus on a single model, CESM1, which has preindustrial control runs of sufficient length for a FCM and a sister SOM, in which the slab layer depth has a realistic (time mean) heat capacity. Our result might be different using a different FCM and sister SOM. The impact of ocean dynamics on SST variations is likely underestimated in coarse resolution models, such as those analyzed here, as currents are too broad and weak.

*Acknowledgments.* OG was funded by the NASA Physical Oceanography Program (NNX17AH49G), NOAA ESS Program (NA16OAR4310167), and NOAA OAR Climate Program Office (NA20OAR4310401). MWB was funded by the NSF Physical Oceanography Program (2219707), NOAA ESS Program (NA16OAR4310167 and NA20OAR4310396), and NASA Physical Oceanography Program (NNX17AH49G and 80NSSC20K0823). TD was funded by NOAA OAR Climate Program Office (NA20OAR4310401). The authors are grateful to A. Clement and J. Klavans for lively discussion and help with data access. We also thank S. Larson, K. McMonigal, R. Wills, L. Trenary, B. Huang, N. Vinogradova, L. Li, and Y. Garuba for sharing their insights with us.

*Data availability statement.* All CESM LENS data are available at https://www.cesm.ucar.edu/projects/community-projects/LENS/.

## APPENDIX

### EOF Truncation

We choose 30 EOFs as our truncation for CDA because for truncations of 30 EOFs or more, our results regarding the significance and structure of the discriminants do not depend on truncation choice, although the order of the components does depend slightly on truncation (Fig. A1, middle and right panels). This order switching is particularly true for SOM-SST-2 and SOM-SST-3, which is an expected consequence of the fact that their variance ratios are close to each other (see Fig. 3) and hence may not be separable. Based on correlations between variates at different truncations, SOM-SST-2 and SOM-SST-3 maintain their identities from 40 to 30 EOFs but switch order from 40 to 20 EOFs. Also, at 20 EOFs, FCM-SST-2 is insignificant (not shown; $\lambda = 1.1$). Nevertheless, the leading SST modes are robust and do not vary depending on EOF truncation choice (see row 1 for SOM-SST-1 and row 4 for FCM-SST-1 in Fig. A1).

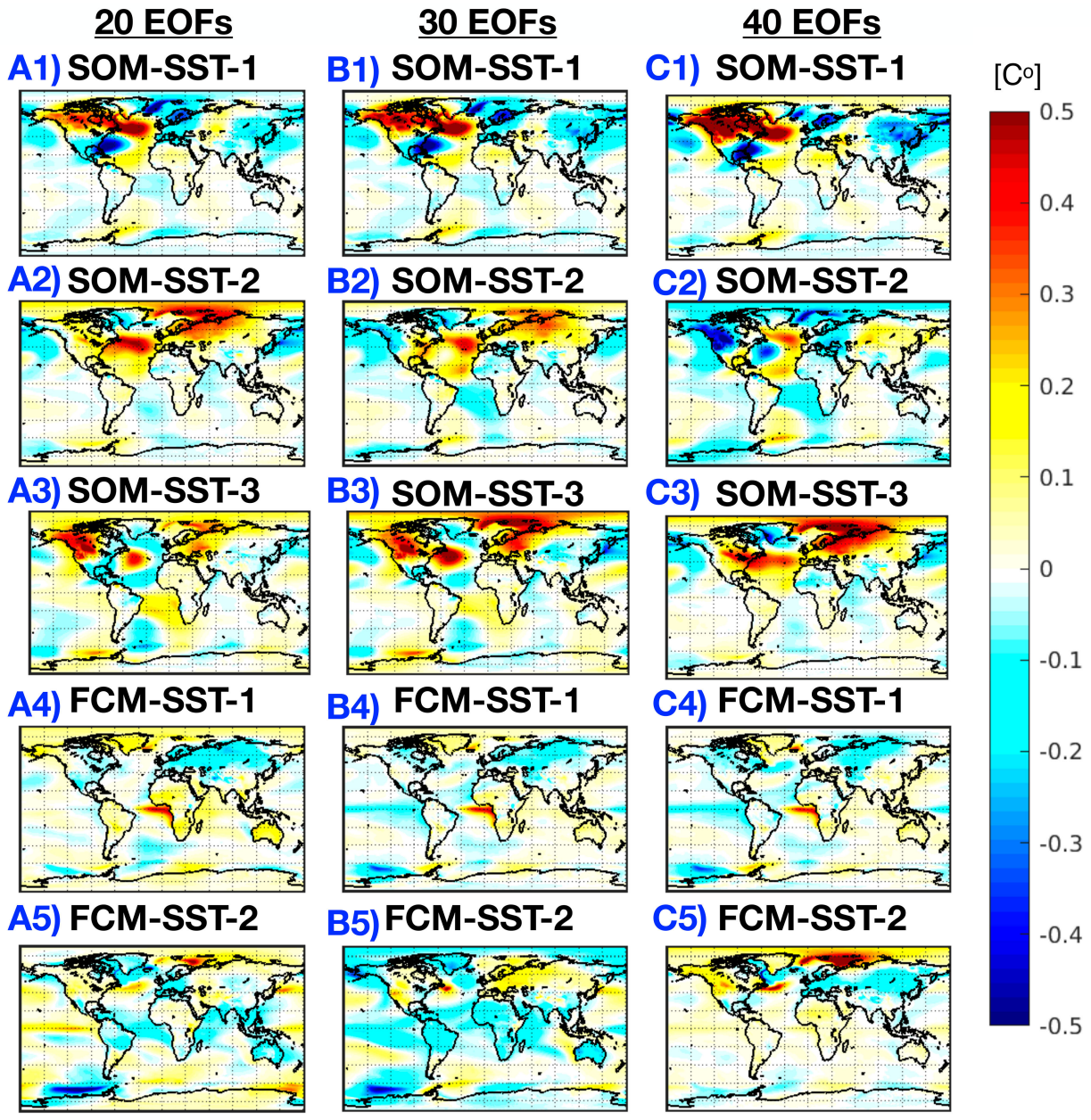


FIG. A1. Regression patterns of the five leading SST modes onto ST for different EOF truncation choices. For slab modes, the regressions are computed with the SOM variate time series onto SOM ST, and for coupled modes, we regress the FCM variate onto FCM ST. A truncation of (left) 20 EOFs, (middle) 30 EOFs, and (right) 40 EOFs are shown.

## REFERENCES

Bellomo, K., L. N. Murphy, M. A. Cane, A. C. Clement, and L. M. Polvani, 2018: Historical forcings as main drivers of the Atlantic multidecadal variability in the CESM large ensemble. *Climate Dyn.*, **50**, 3687–3698, https://doi.org/10.1007/s00382-017-3834-3.

Bishop, S. P., R. J. Small, F. O. Bryan, and R. A. Tomas, 2017: Scale dependence of midlatitude air–sea interaction. *J. Climate*, **30**, 8207–8221, https://doi.org/10.1175/JCLI-D-17-0159.1.

Böning, C. W., M. Scheinert, J. Dengg, A. Biastoch, and A. Funk, 2006: Decadal variability of subpolar gyre transport and its reverberation in the North Atlantic overturning. *Geophys. Res. Lett.*, **33**, L21S01, https://doi.org/10.1029/2006GL026906.

Booth, B. B. B., N. J. Dunstone, P. R. Halloran, T. Andrews, and N. Bellouin, 2012: Aerosols implicated as a prime driver of twentieth-century North Atlantic climate variability. *Nature*, **484**, 228–232, https://doi.org/10.1038/nature10946.

Buckley, M. W., and J. Marshall, 2016: Observations, inferences, and mechanisms of the Atlantic meridional overturning circulation: A review. *Rev. Geophys.*, **54**, 5–63, https://doi.org/10.1002/2015RG000493.

——, R. M. Ponte, G. Forget, and P. Heimbach, 2014: Low-frequency SST and upper-ocean heat content variability in the North Atlantic. *J. Climate*, **27**, 4996–5018, https://doi.org/10.1175/JCLI-D-13-00316.1.

——, ——, ——, and ——, 2015: Determining the origins of advective heat transport convergence variability in the North Atlantic. *J. Climate*, **28**, 3943–3956, https://doi.org/10.1175/JCLI-D-14-00579.1.

Cane, M. A., A. C. Clement, L. N. Murphy, and K. Bellomo, 2017: Low-pass filtering, heat flux, and Atlantic multidecadal variability. *J. Climate*, **30**, 7529–7553, https://doi.org/10.1175/JCLI-D-16-0810.1.

Cassou, C., C. Deser, L. Terray, J. W. Hurrell, and M. Drévillon, 2004: Summer sea surface temperature conditions in the North Atlantic and their impact upon the atmospheric circulation in early winter. *J. Climate*, **17**, 3349–3363, https://doi.org/10.1175/1520-0442(2004)017<3349:SSSTCI>2.0.CO;2.

Cayan, D. R., 1992a: Latent and sensible heat flux anomalies over the northern oceans: Driving the sea surface temperature. *J. Phys. Oceanogr.*, **22**, 859–881, https://doi.org/10.1175/1520-0485(1992)022<0859:LASHFA>2.0.CO;2.

——, 1992b: Latent and sensible heat flux anomalies over the northern oceans: The connection to monthly atmospheric circulation. *J. Climate*, **5**, 354–369, https://doi.org/10.1175/1520-0442(1992)005<0354:LASHFA>2.0.CO;2.

Clement, A., P. DiNezio, and C. Deser, 2011: Rethinking the ocean's role in the Southern Oscillation. *J. Climate*, **24**, 4056–4072, https://doi.org/10.1175/2011JCLI3973.1.

——, K. Bellomo, L. N. Murphy, M. A. Cane, T. Mauritsen, G. Rädel, and B. Stevens, 2015: The Atlantic multidecadal oscillation without a role for ocean circulation. *Science*, **350**, 320–324, https://doi.org/10.1126/science.aab3980.

Cook, E. R., Y. Kushnir, J. E. Smerdon, A. P. Williams, K. J. Anchukaitis, and E. R. Wahl, 2019: A Euro-Mediterranean tree-ring reconstruction of the winter NAO index since 910 C.E. *Climate Dyn.*, **53**, 1567–1580, https://doi.org/10.1007/s00382-019-04696-2.

Danabasoglu, G., W. G. Large, and B. P. Briegleb, 2010: Climate impacts of parameterized Nordic Sea overflows. *J. Geophys. Res.*, **115**, C11005, https://doi.org/10.1029/2010JC006243.

——, S. C. Bates, B. P. Briegleb, S. R. Jayne, M. Jochum, W. G. Large, S. Peacock, and S. G. Yeager, 2012a: The CCSM4 ocean component. *J. Climate*, **25**, 1361–1389, https://doi.org/10.1175/JCLI-D-11-00091.1.

——, S. G. Yeager, Y.-O. Kwon, J. J. Tribbia, A. S. Phillips, and J. W. Hurrell, 2012b: Variability of the Atlantic meridional overturning circulation in CCSM4. *J. Climate*, **25**, 5153–5172, https://doi.org/10.1175/JCLI-D-11-00463.1.

——, L. Landrum, S. G. Yeager, and P. R. Gent, 2019: Robust and nonrobust aspects of Atlantic meridional overturning circulation variability and mechanisms in the Community Earth System Model. *J. Climate*, **32**, 7349–7368, https://doi.org/10.1175/JCLI-D-19-0026.1.

Day, J. J., J. C. Hargreaves, J. D. Annan, and A. Abe-Ouchi, 2012: Sources of multi-decadal variability in Arctic sea ice extent. *Environ. Res. Lett.*, **7**, 034011, https://doi.org/10.1088/1748-9326/7/3/034011.

de Coëtlogon, G., and C. Frankignoul, 2003: The persistence of winter sea surface temperature in the North Atlantic. *J. Climate*, **16**, 1364–1377, https://doi.org/10.1175/1520-0442(2003)16%3C1364:TPOWSS%3E2.0.CO;2.

DelSole, T., and M. Tippett, 2022: *Statistical Methods for Climate Scientists*. Cambridge University Press, 542 pp.

Delworth, T. L., R. Zhang, and M. E. Mann, 2007: Decadal to centennial variability of the Atlantic from observations and models. *Ocean Circulation: Mechanisms and Impacts—Past and Future Changes of Meridional Overturning*, *Geophys. Monogr.*, Vol. 173, Amer. Geophys. Union, 131–148, https://doi.org/10.1029/173GM10.

——, F. Zeng, L. Zhang, R. Zhang, G. A. Vecchi, and X. Yang, 2017: The central role of ocean dynamics in connecting the North Atlantic Oscillation to the extratropical component of the Atlantic multidecadal oscillation. *J. Climate*, **30**, 3789–3805, https://doi.org/10.1175/JCLI-D-16-0358.1.

Desbruyères, D., L. Chafik, and G. Maze, 2021: A shift in the ocean circulation has warmed the subpolar North Atlantic Ocean since 2016. *Commun. Earth Environ.*, **2**, 48, https://doi.org/10.1038/s43247-021-00120-y.

Deser, C., and A. S. Phillips, 2021: Defining the internal component of Atlantic multidecadal variability in a changing climate. *Geophys. Res. Lett.*, **48**, e2021GL095023, https://doi.org/10.1029/2021GL095023.

Dippe, T., R. J. Greatbatch, and H. Ding, 2018: On the relationship between Atlantic Niño variability and ocean dynamics. *Climate Dyn.*, **51**, 597–612, https://doi.org/10.1007/s00382-017-3943-z.

Dommenget, D., 2010: The slab ocean El Niño. *Geophys. Res. Lett.*, **37**, L20701, https://doi.org/10.1029/2010GL044888.

Enfield, D. B., A. M. Mestas-Nuñez, and P. J. Trimble, 2001: The Atlantic multidecadal oscillation and its relation to rainfall and river flows in the continental U.S. *Geophys. Res. Lett.*, **28**, 2077–2080, https://doi.org/10.1029/2000GL012745.

Folland, C. K., T. N. Palmer, and D. E. Parker, 1986: Sahel rainfall and worldwide sea temperatures, 1901–85. *Nature*, **320**, 602–607, https://doi.org/10.1038/320602a0.

Foltz, G. R., and M. J. McPhaden, 2010: Interaction between the Atlantic meridional and Niño modes. *Geophys. Res. Lett.*, **37**, L18604, https://doi.org/10.1029/2010GL044001.

Frankignoul, C., 1985: Sea surface temperature anomalies, planetary waves, and air-sea feedback in the middle latitudes. *Rev. Geophys.*, **23**, 357–390, https://doi.org/10.1029/RG023i004p00357.

——, and K. Hasselmann, 1977: Stochastic climate models, Part II Application to sea-surface temperature anomalies and thermocline variability. *Tellus*, **29**, 289–305, https://doi.org/10.3402/tellusa.v29i4.11362.

——, and E. Kestenare, 2005: Observed Atlantic SST anomaly impact on the NAO: An update. *J. Climate*, **18**, 4089–4094, https://doi.org/10.1175/JCLI3523.1.

——, ——, and J. Mignot, 2002: The surface heat flux feedback. Part II: Direct and indirect estimates in the ECHAM4/OPA8 coupled GCM. *Climate Dyn.*, **19**, 649–655, https://doi.org/10.1007/s00382-002-0253-9.

Gastineau, G., and C. Frankignoul, 2014: Influence of the North Atlantic SST variability on the atmospheric circulation during the twentieth century. *J. Climate*, **28**, 1396–1416, https://doi.org/10.1175/JCLI-D-14-00424.1.

Goldenberg, S. B., C. W. Landsea, A. M. Mestas-Nuñez, and W. M. Gray, 2001: The recent increase in Atlantic hurricane activity: Causes and implications. *Science*, **293**, 474–479, https://doi.org/10.1126/science.1060040.

Goodman, J., and J. Marshall, 1999: A model of decadal middle-latitude atmosphere–ocean coupled modes. *J. Climate*, **12**, 621–641, https://doi.org/10.1175/1520-0442(1999)012<0621:AMODML>2.0.CO;2.

Gray, S. T., L. J. Graumlich, J. L. Betancourt, and G. T. Pederson, 2004: A tree-ring based reconstruction of the Atlantic

multidecadal oscillation since 1567 A.D. *Geophys. Res. Lett.*, **31**, L12205, https://doi.org/10.1029/2004GL019932.

Häkkinen, S., and P. B. Rhines, 2004: Decline of subpolar North Atlantic circulation during the 1990s. *Science*, **304**, 555–559, https://doi.org/10.1126/science.1094917.

——, and ——, 2009: Shifting surface currents in the northern North Atlantic Ocean. *J. Geophys. Res.*, **114**, C04005, https://doi.org/10.1029/2008JC004883.

——, ——, and D. L. Worthen, 2011: Warm and saline events embedded in the meridional circulation of the northern North Atlantic. *J. Geophys. Res.*, **116**, C03006, https://doi.org/10.1029/2010JC006275.

Holliday, N. P., and Coauthors, 2008: Reversal of the 1960s to 1990s freshening trend in the northeast North Atlantic and Nordic Seas. *Geophys. Res. Lett.*, **35**, L03614, https://doi.org/10.1029/2007GL032675.

——, S. A. Cunningham, C. Johnson, S. F. Gary, C. Griffiths, J. F. Read, and T. Sherwin, 2015: Multidecadal variability of potential temperature, salinity, and transport in the eastern subpolar North Atlantic. *J. Geophys. Res. Oceans*, **120**, 5945–5967, https://doi.org/10.1002/2015JC010762.

Huang, B., and Coauthors, 2017: Extended Reconstructed Sea Surface Temperature, version 5 (ERSSTv5): Upgrades, validations, and intercomparisons. *J. Climate*, **30**, 8179–8205, https://doi.org/10.1175/JCLI-D-16-0836.1.

Hunke, E. C., 2010: Thickness sensitivities in the CICE sea ice model. *Ocean Modell.*, **34**, 137–149, https://doi.org/10.1016/j.ocemod.2010.05.004.

Hurrell, J. W., 1995: Decadal trends in the North Atlantic Oscillation: Regional temperatures and precipitation. *Science*, **269**, 676–679, https://doi.org/10.1126/science.269.5224.676.

——, Y. Kushnir, G. Ottersen, and M. Visbeck, 2003: An overview of the North Atlantic Oscillation. *The North Atlantic Oscillation: Climatic Significance and Environmental Impact*, *Geophys. Monogr.*, Vol. 134, Amer. Geophys. Union, 1–36, https://doi.org/10.1029/134GM01.

——, and Coauthors, 2013: The Community Earth System Model: A framework for collaborative research. *Bull. Amer. Meteor. Soc.*, **94**, 1339–1360, https://doi.org/10.1175/BAMS-D-12-00121.1.

Kalnay, E., and Coauthors, 1996: The NCEP/NCAR 40-Year Reanalysis Project. *Bull. Amer. Meteor. Soc.*, **77**, 437–472, https://doi.org/10.1175/1520-0477(1996)077<0437:TNYRP>2.0.CO;2.

Karnauskas, K. B., L. Zhang, and D. J. Amaya, 2021: The atmospheric response to North Atlantic SST trends, 1870–2019. *Geophys. Res. Lett.*, **48**, e2020GL090677, https://doi.org/10.1029/2020GL090677.

Kay, J. E., and Coauthors, 2015: The Community Earth System Model (CESM) large ensemble project: A community resource for studying climate change in the presence of internal climate variability. *Bull. Amer. Meteor. Soc.*, **96**, 1333–1349, https://doi.org/10.1175/BAMS-D-13-00255.1.

Keenlyside, N. S., and M. Latif, 2007: Understanding equatorial Atlantic interannual variability. *J. Climate*, **20**, 131–142, https://doi.org/10.1175/JCLI3992.1.

Kerr, R. A., 2000: A North Atlantic climate pacemaker for the centuries. *Science*, **288**, 1984–1985, https://doi.org/10.1126/science.288.5473.1984.

Kim, W. M., S. Yeager, P. Chang, and G. Danabasoglu, 2018: Low-frequency North Atlantic climate variability in the Community Earth System Model large ensemble. *J. Climate*, **31**, 787–813, https://doi.org/10.1175/JCLI-D-17-0193.1.

——, ——, and G. Danabasoglu, 2019: Atlantic multidecadal variability and associated climate impacts initiated by ocean thermohaline dynamics. *J. Climate*, **33**, 1317–1334, https://doi.org/10.1175/JCLI-D-19-0530.1.

Knight, J. R., C. K. Folland, and A. A. Scaife, 2006: Climate impacts of the Atlantic multidecadal oscillation. *Geophys. Res. Lett.*, **33**, L17706, https://doi.org/10.1029/2006GL026242.

Knudsen, M. F., M.-S. Seidenkrantz, B. H. Jacobsen, and A. Kuijpers, 2011: Tracking the Atlantic multidecadal oscillation through the last 8,000 years. *Nat. Commun.*, **2**, 178, https://doi.org/10.1038/ncomms1186.

Kullback, S., 1997: *Information Theory and Statistics*. Courier Corporation, 399 pp.

Kushnir, Y., 1994: Interdecadal variations in North Atlantic sea surface temperature and associated atmospheric conditions. *J. Climate*, **7**, 141–157, https://doi.org/10.1175/1520-0442(1994)007<0141:IVINAS>2.0.CO;2.

Larson, S. M., M. W. Buckley, and A. C. Clement, 2020: Extracting the buoyancy-driven Atlantic meridional overturning circulation. *J. Climate*, **33**, 4697–4714, https://doi.org/10.1175/JCLI-D-19-0590.1.

Lawrence, D. M., and Coauthors, 2019: The community land model version 5: Description of new features, benchmarking, and impact of forcing uncertainty. *J. Adv. Model. Earth Syst.*, **11**, 4245–4287, https://doi.org/10.1029/2018MS001583.

Li, L., M. S. Lozier, and M. W. Buckley, 2020: An investigation of the ocean's role in Atlantic multidecadal variability. *J. Climate*, **33**, 3019–3035, https://doi.org/10.1175/JCLI-D-19-0236.1.

Liu, G., Y.-O. Kwon, C. Frankignoul, and J. Lu, 2023: Understanding the drivers of Atlantic multidecadal variability using a stochastic model hierarchy. *J. Climate*, **36**, 1043–1058, https://doi.org/10.1175/JCLI-D-22-0309.1.

Liu, Z., P. Gu, and T. L. Delworth, 2023: Strong red noise ocean forcing on Atlantic multidecadal variability assessed from surface heat flux: Theory and application. *J. Climate*, **36**, 55–80, https://doi.org/10.1175/JCLI-D-22-0063.1.

Lübbecke, J., and M. McPhaden, 2017: Is the Atlantic Niño mode as asymmetric as ENSO? *Geophysical Research Abstracts*, Vol. 19, Abstract 3181, https://meetingorganizer.copernicus.org/EGU2017/EGU2017-3181.pdf.

Manabe, S., and R. J. Stouffer, 1988: Two stable equilibria of a coupled ocean–atmosphere model. *J. Climate*, **1**, 841–866, https://doi.org/10.1175/1520-0442(1988)001<0841:TSEOAC>2.0.CO;2.

Mann, M. E., B. A. Steinman, D. J. Brouillette, and S. K. Miller, 2021: Multidecadal climate oscillations during the past millennium driven by volcanic forcing. *Science*, **371**, 1014–1019, https://doi.org/10.1126/science.abc5810.

Mignot, J., and C. Frankignoul, 2003: On the interannual variability of surface salinity in the Atlantic. *Climate Dyn.*, **20**, 555–565, https://doi.org/10.1007/s00382-002-0294-0.

Murphy, L. N., K. Bellomo, M. Cane, and A. Clement, 2017: The role of historical forcings in simulating the observed Atlantic multidecadal oscillation. *Geophys. Res. Lett.*, **44**, 2472–2480, https://doi.org/10.1002/2016GL071337.

——, J. M. Klavans, A. C. Clement, and M. A. Cane, 2021: Investigating the roles of external forcing and ocean circulation on the Atlantic multidecadal SST variability in a large ensemble climate model hierarchy. *J. Climate*, **34**, 4835–4849, https://doi.org/10.1175/JCLI-D-20-0167.1.

Neale, R. B., and Coauthors, 2010: Description of the NCAR Community Atmosphere Model (CAM 5.0). NCAR Tech.

Note NCAR/TN-486+STR, 268 pp., http://www.cesm.ucar.edu/models/cesm1.1/cam/docs/description/cam5_desc.pdf.

Nigam, S., A. Ruiz-Barradas, and L. Chafik, 2018: Gulf Stream excursions and sectional detachments generate the decadal pulses in the Atlantic multidecadal oscillation. *J. Climate*, **31**, 2853–2870, https://doi.org/10.1175/JCLI-D-17-0010.1.

Oelsmann, J., L. Borchert, R. Hand, J. Baehr, and J. H. Jungclaus, 2020: Linking ocean forcing and atmospheric interactions to Atlantic multidecadal variability in MPI-ESM1.2. *Geophys. Res. Lett.*, **47**, e2020GL087259, https://doi.org/10.1029/2020GL087259.

O'Reilly, C. H., M. Huber, T. Woollings, and L. Zanna, 2016: The signature of low-frequency oceanic forcing in the Atlantic multidecadal oscillation. *Geophys. Res. Lett.*, **43**, 2810–2818, https://doi.org/10.1002/2016GL067925.

Peings, Y., and G. Magnusdottir, 2016: Wintertime atmospheric response to Atlantic multidecadal variability: Effect of stratospheric representation and ocean–atmosphere coupling. *Climate Dyn.*, **47**, 1029–1047, https://doi.org/10.1007/s00382-015-2887-4.

Piecuch, C. G., R. M. Ponte, C. M. Little, M. W. Buckley, and I. Fukumori, 2017: Mechanisms underlying recent decadal changes in subpolar North Atlantic Ocean heat content. *J. Geophys. Res. Oceans*, **122**, 7181–7197, https://doi.org/10.1002/2017JC012845.

Pierce, D. W., T. P. Barnett, N. Schneider, R. Saravanan, D. Dommenget, and M. Latif, 2001: The role of ocean dynamics in producing decadal climate variability in the North Pacific. *Climate Dyn.*, **18**, 51–70, https://doi.org/10.1007/s003820100158.

Prodhomme, C., A. Voldoire, E. Exarchou, A.-L. Deppenmeier, J. García-Serrano, and V. Guemas, 2019: How does the seasonal cycle control equatorial Atlantic interannual variability? *Geophys. Res. Lett.*, **46**, 916–922, https://doi.org/10.1029/2018GL080837.

Ruprich-Robert, Y., R. Msadek, F. Castruccio, S. Yeager, T. Delworth, and G. Danabasoglu, 2017: Assessing the climate impacts of the observed Atlantic multidecadal variability using the GFDL CM2.1 and NCAR CESM1 global coupled models. *J. Climate*, **30**, 2785–2810, https://doi.org/10.1175/JCLI-D-16-0127.1.

Schneider, E. K., B. P. Kirtman, and N. Perlin, 2023: The role of atmospheric noise in decadal SST variability. *J. Climate*, **36**, 2147–2166, https://doi.org/10.1175/JCLI-D-22-0399.1.

Seager, R., Y. Kushnir, M. Visbeck, N. Naik, J. Miller, G. Krahmann, and H. Cullen, 2000: Causes of Atlantic Ocean climate variability between 1958 and 1998. *J. Climate*, **13**, 2845–2862, https://doi.org/10.1175/1520-0442(2000)013<2845:COAOCV>2.0.CO;2.

——, ——, P. Chang, N. Naik, J. Miller, and W. Hazeleger, 2001: Looking for the role of the ocean in tropical Atlantic decadal climate variability. *J. Climate*, **14**, 638–655, https://doi.org/10.1175/1520-0442(2001)014<0638:LFTROT>2.0.CO;2.

Silva, P., I. Wainer, and M. Khodri, 2021: Changes in the equatorial mode of the tropical Atlantic in terms of the Bjerknes feedback index. *Climate Dyn.*, **56**, 3005–3024, https://doi.org/10.1007/s00382-021-05627-w.

Small, R. J., F. O. Bryan, S. P. Bishop, and R. A. Tomas, 2019: Air–sea turbulent heat fluxes in climate models and observational analyses: What drives their variability? *J. Climate*, **32**, 2397–2421, https://doi.org/10.1175/JCLI-D-18-0576.1.

Smith, R., and Coauthors, 2010: The Parallel Ocean Program (POP) reference manual ocean component of The Community Climate System Model (CCSM) and Community Earth System Model (CESM). LAUR-10-01853, 141 pp., https://www2.cesm.ucar.edu/models/cesm1.0/pop2/doc/sci/POPRefManual.pdf.

Sukhonos, P. A., and M. A. Alexander, 2023: The reemergence of the winter sea surface temperature tripole in the North Atlantic from ocean reanalysis data. *Climate Dyn.*, **61**, 449–460, https://doi.org/10.1007/s00382-022-06581-x.

Sutton, R. T., and D. L. R. Hodson, 2005: Atlantic Ocean forcing of North American and European summer climate. *Science*, **309**, 115–118, https://doi.org/10.1126/science.1109496.

Ting, M., Y. Kushnir, R. Seager, and C. Li, 2011: Robust features of Atlantic multi-decadal variability and its climate impacts. *Geophys. Res. Lett.*, **38**, L17705, https://doi.org/10.1029/2011GL048712.

Undorf, S., M. A. Bollasina, B. B. B. Booth, and G. C. Hegerl, 2018: Contrasting the effects of the 1850–1975 increase in sulphate aerosols from North America and Europe on the Atlantic in the CESM. *Geophys. Res. Lett.*, **45**, 11 930–11 940, https://doi.org/10.1029/2018GL079970.

Vecchi, G. A., T. L. Delworth, and B. Booth, 2017: Climate science: Origins of Atlantic decadal swings. *Nature*, **548**, 284–285, https://doi.org/10.1038/nature23538.

Wen, N., Z. Liu, Q. Liu, and C. Frankignoul, 2005: Observations of SST, heat flux and North Atlantic Ocean–atmosphere interaction. *Geophys. Res. Lett.*, **32**, L24619, https://doi.org/10.1029/2005GL024871.

Wills, R. C., K. C. Armour, D. S. Battisti, and D. L. Hartmann, 2019: Ocean–atmosphere dynamical coupling fundamental to the Atlantic multidecadal oscillation. *J. Climate*, **32**, 251–272, https://doi.org/10.1175/JCLI-D-18-0269.1.

Wills, S. M., D. W. J. Thompson, and L. M. Ciasto, 2016: On the observed relationships between variability in Gulf Stream sea surface temperatures and the atmospheric circulation over the North Atlantic. *J. Climate*, **29**, 3719–3730, https://doi.org/10.1175/JCLI-D-15-0820.1.

Xie, S.-P., and J. A. Carton, 2004: Tropical Atlantic variability: Patterns, mechanisms, and impacts. *Earth Climate: The Ocean-Atmosphere Interaction*, *Geophys. Monogr.*, Vol. 147, Amer. Geophys. Union, 121–142, https://doi.org/10.1029/147GM07.

Yan, X., R. Zhang, and T. R. Knutson, 2019: A multivariate AMV index and associated discrepancies between observed and CMIP5 externally forced AMV. *Geophys. Res. Lett.*, **46**, 4421–4431, https://doi.org/10.1029/2019GL082787.

Zebiak, S. E., 1993: Air–sea interaction in the equatorial Atlantic region. *J. Climate*, **6**, 1567–1586, https://doi.org/10.1175/1520-0442(1993)006<1567:AIITEA>2.0.CO;2.

Zhang, D., R. Sutton, G. Danabasoglu, T. L. Delworth, W. M. Kim, J. Robson, and S. G. Yeager, 2016: Comment on "The Atlantic multidecadal oscillation without a role for ocean circulation". *Science*, **352**, 1527–1527, https://doi.org/10.1126/science.aaf1660.

Zhang, H., A. Clement, and P. Di Nezio, 2014: The South Pacific meridional mode: A mechanism for ENSO-like variability. *J. Climate*, **27**, 769–783, https://doi.org/10.1175/JCLI-D-13-00082.1.

Zhang, J., and R. Zhang, 2015: On the evolution of Atlantic meridional overturning circulation fingerprint and implications for decadal predictability in the North Atlantic. *Geophys. Res. Lett.*, **42**, 5419–5426, https://doi.org/10.1002/2015GL064596.

Zhang, L., and C. Wang, 2013: Multidecadal North Atlantic sea surface temperature and Atlantic meridional overturning circulation variability in CMIP5 historical simulations. *J.*

*Geophys. Res. Oceans*, **118**, 5772–5791, https://doi.org/10.1002/jgrc.20390.

Zhang, R., 2015: Mechanisms for low-frequency variability of summer Arctic sea ice extent. *Proc. Natl. Acad. Sci. USA*, **112**, 4570–4575, https://doi.org/10.1073/pnas.1422296112.

——, 2017: On the persistence and coherence of subpolar sea surface temperature and salinity anomalies associated with the Atlantic multidecadal variability. *Geophys. Res. Lett.*, **44**, 7865–7875, https://doi.org/10.1002/2017GL074342.

——, R. Sutton, G. Danabasoglu, Y.-O. Kwon, R. Marsh, S. G. Yeager, D. E. Amrhein, and C. M. Little, 2019: A review of the role of the Atlantic meridional overturning circulation in Atlantic multidecadal variability and associated climate impacts. *Rev. Geophys.*, **57**, 316–375, https://doi.org/10.1029/2019RG000644.